12-2017

Flow Assessment Using Optical Coherence Microscopy Based Particle Image Velocimetry

Siyu Ma
Clemson University

Recommended Citation
Ma, Siyu, "Flow Assessment Using Optical Coherence Microscopy Based Particle Image Velocimetry" (2017). *All Dissertations*. 2055.
https://tigerprints.clemson.edu/all_dissertations/2055

FLOW ASSESSMENT USING OPTICAL COHERENCE MICROSCOPY-BASED PARTICLE IMAGE VELOCIMETRY

A Dissertation
Presented to
the Graduate School of
Clemson University

In Partial Fulfillment
of the Requirements for the Degree
Doctor of Philosophy
Bioengineering

---

by
Siyu Ma
December 2017

Accepted by:
Dr. Bruce Z. Gao, Committee Chair
Dr. Delphine Dean
Dr. Hai Yao
Dr. Tong Ye

ABSTRACT

Congenital heart diseases (CHDs) are the most common forms of congenital malformation in newborns. Among all types of CHDs, a large portion is contributed by malformation of endocardial cushion malformation during early heart development. Although the etiology of endocardial cushion malformation is unclear, it is a result of interactions between genetic and environmental factors has been confirmed. There is hypothesis indicating that malformation of endocardial cushion is caused by altered shear stress conditions where in cushion forming area the shear stress is supposed to be high compare with other area in congenital heart. However it is difficult to justify due to lack of in vivo imaging modality that is able to monitor structure and hemodynamic conditions simultaneously and over long time period. To address this problem, we present an optical coherence microscopy based particle image velocimetry system. This system is capable of invasively imaging biological sample structures at micrometer resolution and providing velocity information at the same time. With this imaging set up we successfully assessed velocity profile in a microfluidic system with simultaneous structure details demonstration of the microfluidic channel. Both flow measurement and structural information were verified using conventional microscopy. As a result, OCM-based PIV imaging modality not only makes it feasible to study in detail the process of congenital heart remodeling in response to environmental alterations, but also provides new options for measuring fluid flow in live tissue.

DEDICATION

This work is dedicated to my mother, BEI MA, who helped me to perceive the world in childhood, accompanied me when I worked hard as a student, consulted as a good friend when I was lost, supported with no doubt for all my decisions, and loved me all the time with all her life. I am lucky to have you to be my mother. I will never accomplish anything without you. I love you.

ACHKNOWLEDGEMENT

First of all I would like to thank my advisor, Prof. Bruce Z. Gao, who introduced me into academic research field, taught me the scientific methods of graduate study, and guided me through the way of pursuing research goals. Moreover, I am grateful for his patience and kind comforts when I was going through physiological depression during my fourth year of study. I gained knowledge from him as a teacher, and wisdom from him as a friend.

Second of all I must say thank you to my undergraduate advisor, Prof. Xianfeng Zhu. He changed me from a student that only focused on course works to a researcher that is motivated to learn knowledge by myself and is confident when encountered with problems. He encouraged me to continue graduate study after my graduation from Tianjin University. I would never be a doctor without his mentors.

Thirdly, I am appreciated for Dr. Zhonghai Wang's companion. As my boyfriend he not only offered great assistance to my academic works but also helped in my daily life. I felt safe and belonged when he was with me when we were studying far away from home. He gave me useful suggestions about my study habit to better fit in research field. With his impact I became more self-confident as a person and as a researcher. I felt lucky to have him with me.

Last but not least, I would like to express grate to all my current and previous lab mates. We enjoyed lunch time, shared happy moments, solved research problems, encouraged each other all together during my six years in Clemson. Without you I would be lonely and desperate.

TABLE OF CONTENTS

Table of Contents (continued)

Page

LIST OF FIGURES

Figure Page

List of Figures (continued)

Page

Figure

List of Figures (continued)

Page

Figure

List of Figures (continued)

Page

Figure

List of Figures (continued)

Page

Figure

List of Figures (continued)

Page

Figure

CHAPTER 1 INTRODUCTION

1.1 Scope of research

In this paper, we present a novel imaging modality that combines optical coherence microscopy (OCM) and particle image velocimetry (PIV) to enable structural and functional visualization simultaneously for exploration of pathology of congenital heart disease (CHD) during early embryonic heart development stages. CHD is malformation of heart structures and great vessels that are present at birth. The disease is present in about 1% of live births in the US and in 48.9 million people globally, causing 319,000 deaths in 2015 [1, 2], named as the most common congenital malformation in newborns[3]. The embryonic human heart progresses from a tubular structure that undergoes dramatic morphological and functional changes and finally forms the four chamber architecture. It is during this period of time, especially between the early stages of embryonic heart develop[4], that most CHD originates[5, 6]. Although the etiology of CHD is largely incomplete, it is widely accepted that both genetic and environmental factors are responsible for development of CHD[7-10]. For example, heart septal malformation, a common congenital heart defect, may involve improper gene expression of endothelial cell cilia in response to high shear stress blood flow. This causes failure of transition from endothelial cell to mesenchymal cell and ultimately leads to remodeling of heart morphology and alteration of hemodynamic conditions [11]. To address this issue, a noninvasive imaging technique is needed to assess the interactions of genetic and environmental factors that affect embryonic heart remodeling in vivo. OCM-based PIV imaging modality not only makes it feasible to study in detail the process of congenital heart remodeling in response to environmental alterations, but also provides new options for measuring fluid flow in live tissue.

1.2 **Backgrounds**

During early developmental stages, the straight tube shaped embryonic heart develops into a bended shaped tube, which later evolves into twisted and bended shaped tube [12]. In the twist and bend shaped period, the layer between endocardial cells and myocardial cells in the area of the atrioventricular canal (AV canal) and outflow tract (OFT) thickens, as shown on Figure 1.2, and eventually turns into the cardiac cushion, the primordia of heart valve and septa. The most important procedure involved in this cardiac cushion formation process is termed endocardial mesenchymal transition (EMT).

A detailed explanation of developmental stages of the cardiac cushion, including the process of EMT in AVC area in a mouse embryo, is illustrated in Figure 1.2 [13]. Initially the endocardial endothelial cells (EC) lining the AV canal region delaminate away from myocardium in the same area and protrude toward the lumen. Cardiac jelly is deposited between the endocardium and myocardium, creating a septation. Then EMT occurs as some of the endocardial cells sense stimulation from the environment and detach from neighboring cells, differentiate into mesenchymal cells, and invade the cardiac jelly. With residence and accumulation of mesenchymal cells, the cellularized endocardial cushions fuse to form the AV valvuloseptal complex, which divides ventricular inflow into right (R) and left (L) AV annuli. After further remodeling of mesenchymal cells into fibrous tissue, this portion of heart eventually forms the central core of mature valve leaflet tissue. Since

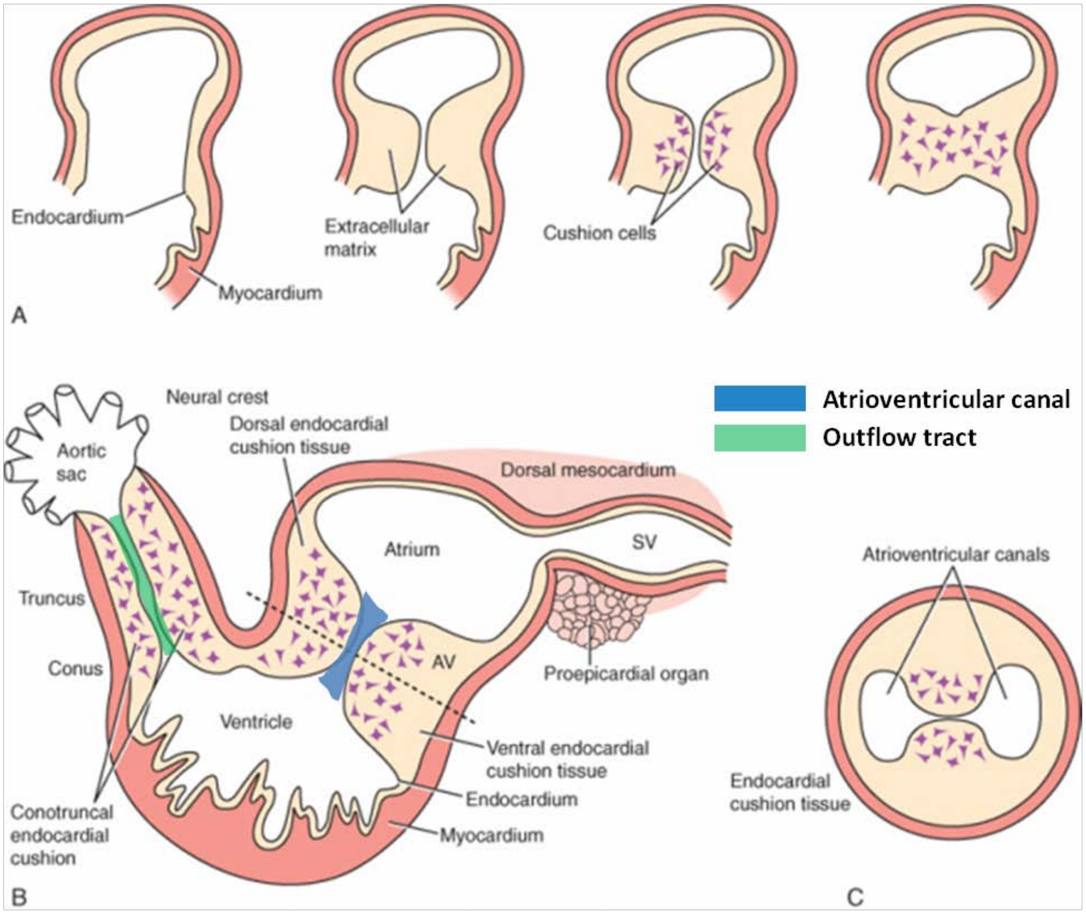

Figure 1.1 Endocardial cushion formation in human embryonic heart. Image adapted from [12] with permission from Elsevier, copyright 2009.

EMT plays a key role in valvular and septal morphogenesis during early embryonic heart development, failure of EMT leads to abnormal development of cardiac valves and septa.

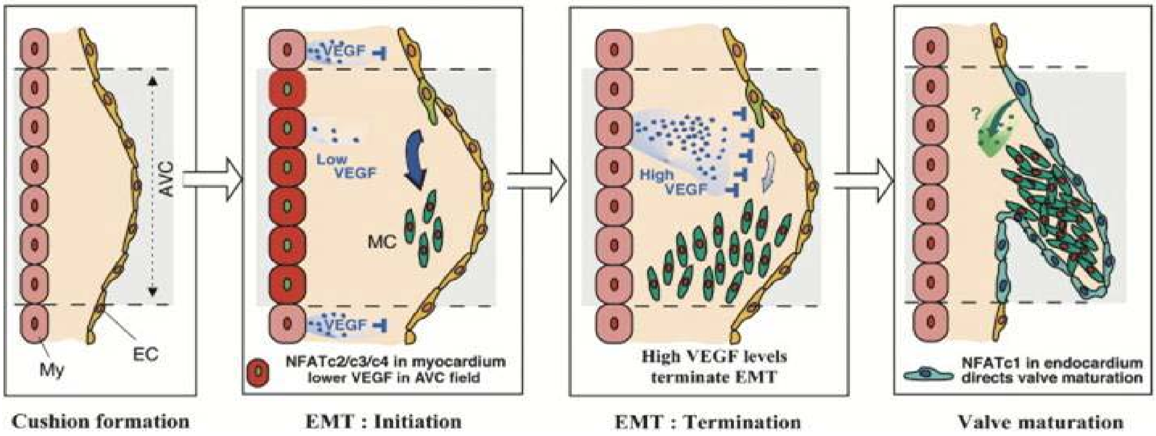

Figure 1.2 Endocardial cushion formation and maturation steps. AVC, Atrioventricular canal; EC, endocardial cell; My, Myocardial cell; MC, mesenchymal cell. Image adapted from [13] with the permission from Elsevier, copyright 2008.

Research has shown that occurrence of EMT is highly related to shear stress via the shear sensing function of the primary cilium lining in the endocardial heart lumen[14]. Primary cilia on ECs have been identified only in the area of low shear stress in the embryonic heart, whereas tissue in the area of the EMT process is devoid of primary cilia [15, 16]. As mechanosensors, primary cilia respond to shear stress by expressing shear responsive genes, including Krüppel-like factor 2 (Klf2), which further coordinate a major part of establishing a quiescent, antithrombotic, anti-inflammatory phenotype of ECs[17, 18] (Figure 1.3). Simultaneously, in the areas that develop the cardiac cushion, the absence of primary cilia leads to failure of increased expression of Klf2 in response to shear stress, which eventually causes a transforming growth factor-beta (Tgfβ)- driven EMT process[14, 19]. The shear stress condition (low or high), presence of primary cilia, and EMT occurrence are closely related to each other. Based on this cause-and-effect chain, we were

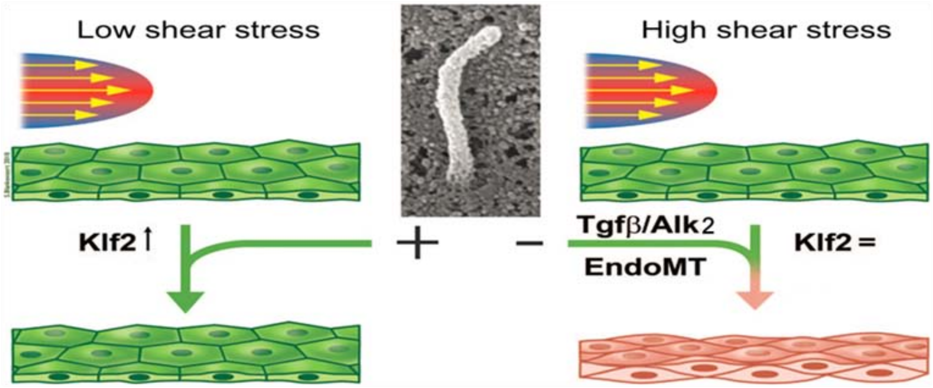

Figure 1.3 Shear induced EMT process. Adapted from[14] with permission from Wolters Kluwer Health, Inc., copyright 2011.

interested in examining whether manual alteration of a previously high shear stress area into a low shear stress area would cause a change of hemodynamic condition leading to failure of the EMT process, which would ultimately result in heart valve and septal malformation.

For this study, we needed an imaging modality capable of visualizing the hemodynamic conditions simultaneously with the morphological adaption to blood flow. This imaging system should be able to provide cellular level resolution in three dimensions to demonstrate structural changes, high frame rate to measure blood flow during embryonic heart development, and over 200 micrometer penetration depth to reconstruct structure and calculate PIV vectors.

High frequency ultrasound biomicroscopy has been reported to visualize the embryonic heart and blood flow. However, insufficient resolution leads to an endocardial layer undistinguishable to blood flow, making hemodynamic conditions difficult to analyze [20]. Although magnetic resonance imaging (MRI) can characterize blood flow based on concentration of blood oxygen [21], to the technique is unable to evaluate the direction of blood flow. Several modification of conventional CT imaging make it feasible to obtain high resolution images for accessing both structure and flow [22-24]. For instance, numerous studies have focused on the application of dynamic CT in evaluating cerebral blood flow [25, 26]. However, the necessity of using a contrast agent that could cause unknown cell-level toxicity responses prevents CT being the suitable technique for live body imaging. Positron emission tomography (PET) provides a noninvasive approach to assessment of blood flow, but it is expensive to operate and difficult to access.

Optical coherence tomography (OCT) has high spatial and temporal resolution for real-time recording of a beating embryonic heart tube with micrometer resolution. It can be used to analyze hemodynamic parameters by generating M-mode scans and calculating blood speed in the direction of axial axis when combined with the Doppler principle (DOCT) [27] . This property is valuable because both morphological and hemodynamic conditions can be monitored simultaneously using the same modality and even the same data. DOCT has been reported to characterize microfluidic systems, including flow in the embryonic heart during early developmental stages [27-30]. However, the result is inaccurate due to phase analysis that provides Doppler velocity signals since the phase term adds intrinsic noise in comparison with intensity analysis that provides only morphological information. Doppler OCT requires multi-angle illumination optics to obtain 2D (i.e., $\vec{v} = v_x\vec{i} + v_z\vec{k}$) and 3D (i.e., $\vec{v} = v_x\vec{i} + v_y\vec{j} + v_z\vec{k}$) velocity vector information. Alternatively, the midline of the vasculature can be used to determine the Doppler angle since flow is confined to well-defined geometries. However, this requires post-acquisition data processing that is slow and lost more accuracy compared with real time two dimensional morphology data.

PIV, an imaging technique specifically invented for flow characterization, is fast and accurate in determining flow velocity with resolution that rivals that of OCM. Nevertheless, PIV uses an illumination light sheet penetrating the sample from the side to generate the particular plane being imaged. This is especially inconvenient when imaging biological tissues since animals are sacrificed and embedded in transparent gel to precisely control position with respect to the light-sheet and the detection lens. OCM is well suited for taking PIV image because the OCM B-scan is geometrically similar to an illumination light sheet except that a higher resolution can be achieved with OCM frame scanning. As a result, the illumination and detection optics are combined when OCM is used for PIV imaging, making it more feasible to evaluate flow in biological tissues when compared with conventional PIV.

1.3 Research goals and specific aims

Our long-term goal is to apply the OCM-based PIV to visualize and quantify the morphology and hemodynamic conditions simultaneously of in vivo samples, such as the embryonic heart tube. The objective of the proposed research is to combine Bessel illumination OCM with PIV to visualize the morphology of microfluidic system with a resolution at the micronmeter level and measure the flow field with seeded particles simultaneously. To build up this bioimaging modality, we will incorporate an axicon lens to create a Bessel illumination that extensively elongate the focusing range of the objective, which for OCM serves as the imaging lens and for PIV serves as the illumination lens. The specific aims are:

Aim 1: Develop the OCM system with a Bessel illumination beam

Micrometer level resolutions in both axial and lateral direction and millimeter level focal range demonstrate the ability of OCM to visualize channel morphology and particles in a flow. The cellular level lateral and axial resolution of this system is achieved by applying a pair of NA=0.3 objectives and photonic crystal fiber to expand spectrum bandwidth respectively. In addition, the focusing range of the objective, which is a compensation of lateral resolution, is extended to fully demonstrate morphology of microfluidic channel by creating a Bessel illumination using axicon lens. This modality is capable of cellular level imaging in the depth range of the entire channel, which is required for PIV imaging.

Aim 2: Modify the OCM to achieve PIV imaging function

Although the imaging mechanism makes it an idea option for PIV imaging, OCM still needs modifications to perform PIV measurements. The dispersion caused by broadening of spectrum will be compensated for with prism pairs and iterative program to maintain cellular level resolution. Two end portions of the scanning area will be disposed to ensure the linearity of scanning wave when the scanning is operating at the speed competent to blood flow. All the modifications aforementioned prepare the OCM modality capable of full field real time PIV imaging in cellular level.

Aim 3: Apply the developed system to a microfluidic system

Owning to the non-destructive property of OCM, the proposed modality has potential application in measuring the lumen structure and fluid flow simultaneously. To imitate blood cells, micro beads will be driven to a self fabricated microfluidic channel to create constant flow as the sample of imaging. The simultaneity of particles in the same sectional image will be realized through post acquisition imaging processing. Cross-correlation will be performed in a self coded program to illustrate velocity mapping. 3D reconstruction of morphology of channel will be performed using a Matlab program.

The OCM-based PIV modality is easier to perform in vivo imaiging in comparison with 3D PIV and embracing higher resolution in comparison with Doppler OCT, therefore it provides new option for the field of characterizing flow and structure simultaneously.

1.4 **Significance and innovation**

Among numerous applications of visualizing and quantifying flow velocity, imaging blood flow in the heart tube during embryonic developmental stages is of essential significance and especially challenging. During this period of time, especially during the early stages of embryonic heart development [4], that most congenital heart defects (CHDs) originates[5, 6]. Blood flow, among other factors plays a vital role in altering hemodynamic conditions and remodeling of heart morphology. Our study focused on a noninvasive imaging option to visualize and quantify blood flow and blood vessels simultaneously to better assess how the interactions of genetic and environmental factors affect embryonic heart remodeling in vivo.

The study reported here innovatively combined two imaging techniques, OCM and PIV, to accomplish a new imaging modality that preserved the advantages of each. The advantages of OCM are its noncontact, noninvasive properties inherited from OCT and the capability to provide high resolution in three dimensions and sufficient speed for visualizing microfluidic system morphology and flow velocity. In this study, we incorporate Bessel illumination to extensively elongate the focusing range of the modality, which is the major limitation for conventional OCM. Conventional PIV is accurate in examining flow velocity because it directly measures the displacements of each individual particle in two consecutive images. The combination of these two techniques allows a long period sampling time that includes no destructive process, and eventually results in PIV images with cellular-level resolution, deep penetration, intensity display of microparticles. The OCM-based PIV technique provides a new perspective in visualizing morphology and flow velocity of a fluidic system.

OCT is well suited to particle tracking velocimetry in the application of imaging cilia-driven fluid flow [31]. However, the proposed technique differentiate itself from the other in that by resolving the tracer particle with three dimensional high resolution, the proposed technique allow for precise velocity measurement, while the application in literature concerns about the path of tracer particle, which requires no need to actually resolve the tracer particle.

CHAPTER 2 LITERATURE REVIEW

2.1 **Embryonic heart valve and septa development**

Embryonic chick heart (ECH) was chosen for this study because it has a low cost and is easy to access and because vertebrates share similar structural and functional processes in heart development. Moreover, the dimensions of ECH make it feasible to observe morphological remodeling in vivo using our imaging set. To conveniently designate and detail the process of ECH development, we applied the most commonly used developmental stages of ECH, termed Hamilton Hamburger (HH) stages[4], as depicted in Figure 2.1.

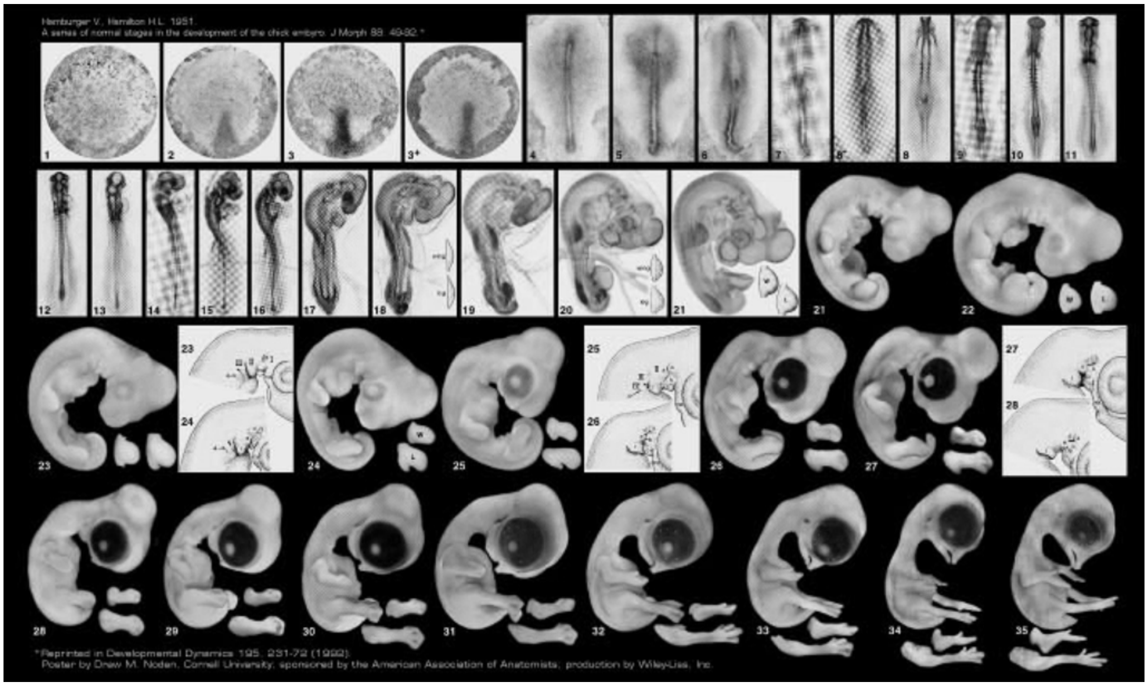

Figure 2.1 Normal stages of chick embryonic development. Numbers indicate HH stages based on external characters, such as numbers of somite pairs (HH1-HH14), limbs

(HH15-HH23), wings, legs, visceral arches (HH24-HH35), and feather germs (after HH36). The correlation between HH stages and chronological ages can be found in Hamburger and Hamilton's work in1951[4]. Image downloaded from http://apps.usd.edu/esci/creation/age/content/natural_clocks/chicken.html and adapted with permission from John Wiley and Sons, copyright 1992

The entire procedure of ECH maturation can be concluded as five phases based on morphogenetic events: pre-looping, dextral-looping, early s-looping, late s-looping, and cardiac septation [5]. During the pre-looping phase (~HH5-9), the embryonic heart lies along the orientation of main body axes. The heart-forming fields in the lateral plate mesoderms are determined, and these later merge themselves into a straight heart tube in front of the developing foregut [5].

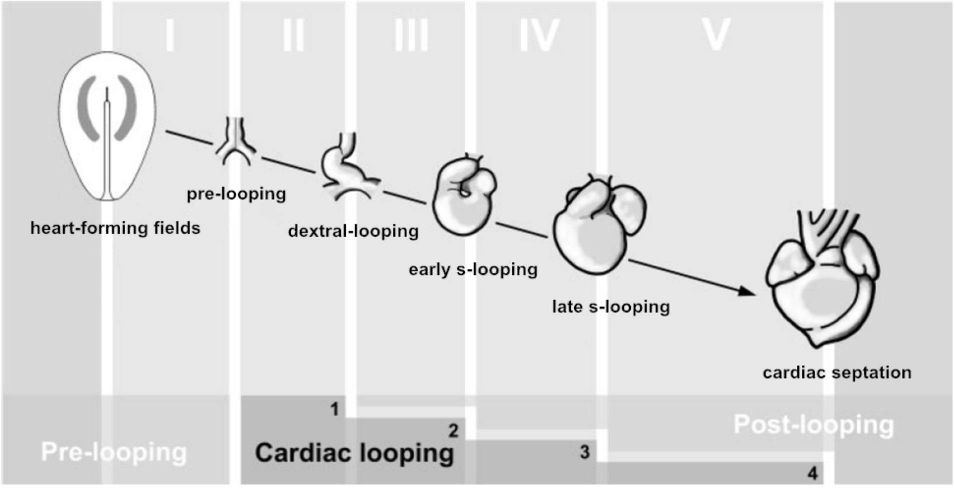

Figure 2.2 Morphogenesis phases of ECH. Images adapted from [5] with permission from John Wiley and Sons, copyright 2008.

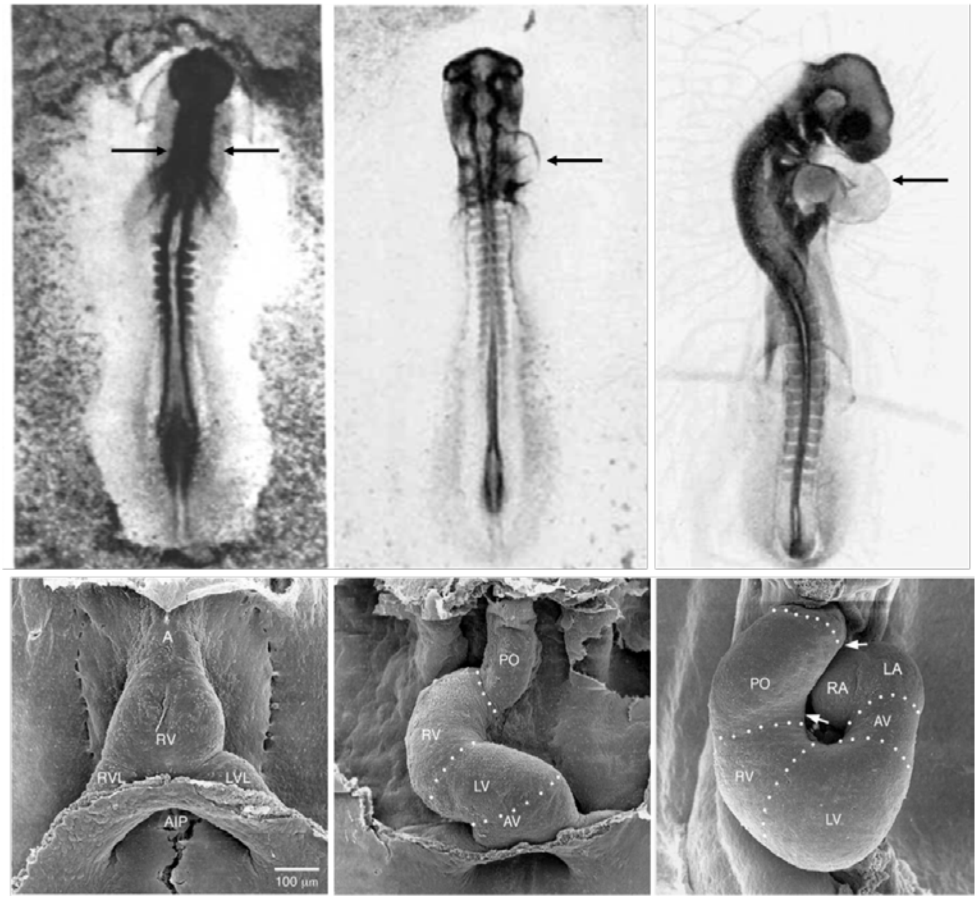

Figure 2.3 Chick embryo and scan electron microscopy (SEM) images of ECH. Left column, pre-looping phase; middle column, dextral-looping phase; right column, early s-looping phase. Black arrows indicate the locations of ECH. A, arterial outlet; RV, embryonic right ventricle; AIP, anterior intestinal portal; PO, proximal part of outflow tract; LV, embryonic left ventricle; RA, right half of the common atrium; LA, left half of the common atrium. Image adapted from [4, 5] with permission from John Wiley and Sons, copyright 1992, 2008.

The most important event of morphogenesis in embryonic heart development is cardiac looping, which includes the three phases after the pre-looping phase. Cardiac looping refers to the sequence of morphological transformations of the embryonic heart from a straight tube into a helically wound loop. Initially at HH9, the ECH establishes itself as a straight, bilaterally nearly symmetrical tube sitting upon a dorsal wall of the primitive pericardial cavity via a bridge tissue, dorsal mesocardium. By subsequent merging of mesocardium, the original heart tube elongates and develops several portions that later evolve into heart-composing elements (from cranial to caudal in direction): arterial outlet connecting with aortic sac, OFT, systemic venous sinus, AVC, and common atrium. Along with elongation of the heart tube, the dorsal mesocardium between arterial and venous poles disappears, and the straight tube transforms its phenotype into a C-shaped loop with convexity points to the right side of the embryo (HH10-12). This C-shaped loop, or dextral looping, establishes the basic type of topological L-R asymmetry of the ventricles. The third phase is the early S-looping phase (HH13-18). It is characterized by the continued bending and twisting of the C-shaped loop such that the distance between arterial and venous poles shortens and the ventricular bend shifts from the cranial to caudal position with respect to the atria. It should be noted that at the end of the early S-looping phase, the proximal OFT is in a primitive position to the right of common atrium, and the AVC and loop are angular at the caudal and cranial borders of the proximal OFT. This is important in the ultimate four chamber structure of mature heart. When the heart proceeds to the late S-looping phase (HH19-24), the proximal OFT shifts leftward to the ventral side of right atrium and the anlage of the great arteries at the arterial pole changes its appearance. Most importantly, the original tubular heart alters its phenotype: The atrial and ventricular segments balloon, creating the primordia of the heart chambers.

The final phase is the cardiac septation phase (HH25-34). It is marked by formation of septal structures that both lumen of future heart and great arterial trunks develop into the pulmonary and systemic blood vessels. This is the final step in heart remodeling with respect to positional relationships of embryonic cardiac segments. These morphogenetic changes include the inner curvature of the ventricular bend, OPT remodeling, and the wedging of the aortic valves.

Cardiac looping plays a key role in embryonic heart development in the following three respects: 1) it initiates the asymmetry of future left and right ventricles; 2) it sets up the approximation of topographical relationships of future heart chambers and great vessels; 3) during this period of time, most CHDs originate and the studies focusing on abnormal cardiac looping provide insights into the etiology of CHDs, which raised enormous attentions for researchers to explore.

Abnormality of heart valves and septa (termed endocardial cushions in the embryonic heart), originate from cardiac looping stages. Immediately after dextral looping (HH10), endocardial cushions form and are populated by valvular precursor cells established from the EMT process described previously. These endocardial cushions undergo directed growth and remodeling to eventually build up the heart valves and septa in the mature heart. In the following part of this section, a detailed discribtion of the cardiac valve and septa formation process will be explained in both morphologic and dynamic perspectives.

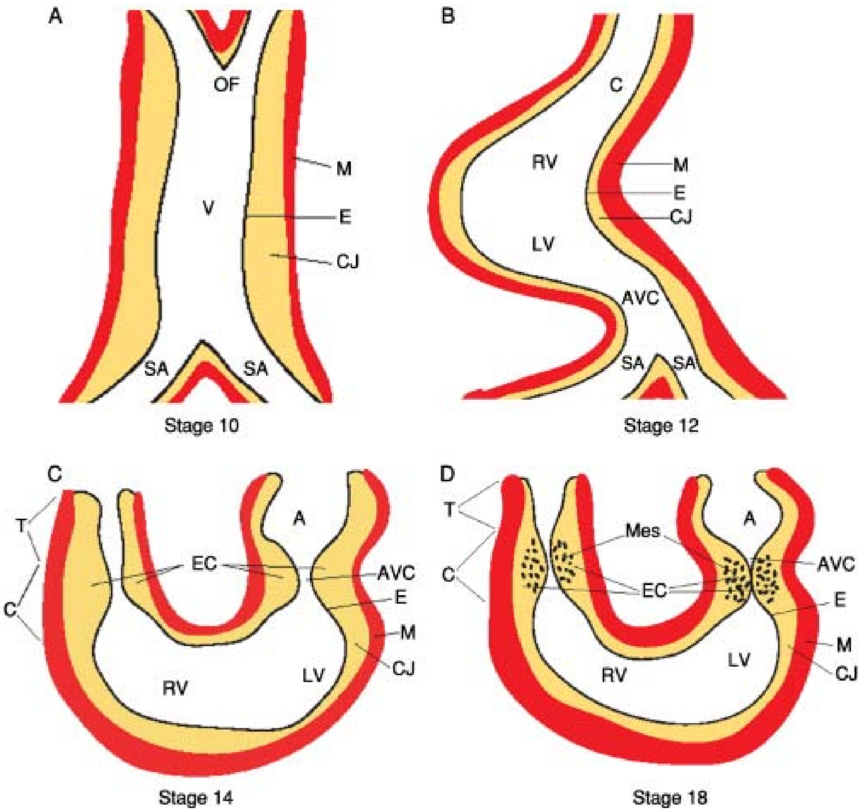

Stage 10

Stage 12

Stage 14

Stage 18

Figure 2.4 Early endocardial cushion development in ECH. OF, outflow tract; V, primitive ventricle; SA, sinus arteriosus; M, myocardial layer; E, endocardial layer, CJ, cardiac jelly; C, conus; RV, right ventricle; LV, left ventricle; T, truncus; EC, endocardial cushion;

A, common atrium; Mes, mesenchymal cells. Image adapted from [32] with permission from Elsevier, copyright 2005.

The straight heart tube consists of two concentric cell layers (Figure 2.4 **A**): the outer myocardium and the inner endocardium. In between is a thin layer of acellular matrix, or cardiac jelly, whose components are mainly secreted by myocardial layer[33] and become integrated from the myocardial side to the endocardial[34]. Localized accumulation of cardiac jelly forms an acellular expansion between endocardial and myocardial layers, the endocardial cushion (Figure 2.4 **C**). Components of the endocardial cushion resemble that of conventional ECM, which includes fibronectin, laminin, collagen, and heparin sulfate proteoglycans. Among these components, fibronectin plays an important role in endocardial cushion formation because it is deposited in a spatiotemporally restricted manner in the AV canal and OFT, thus initiating the active phase of epithelial-mesenchymal interaction at the onset of EMT.

After cushion formation as shown on Figure 2.4 **D** (HH17-HH18), endocardial cells lining the lumen of the AV canal and OFT are activated, transform into mesenchymal phenotypes, and invade the adjacent cardiac cushion. In other areas of the heart, such as the atria and ventricles, the endocardial cells maintain their phenotypes. Initiated by receiving the myocardial-derived inductive stimulus, a series of endocardial changes (EMT) can be described chronologically as [19]: 1) endocardial hypertrophy as a result of Golgi and rough endoplasmic reticulum, 2) cell-cell adhesion loss of endocardial cell, 3) endocardial cell mobility within the layer of epithelium, 4) polarization of expanded Golgi apparatus into the trailing end of future transformed cell, 5) formation of migratory appendages along the basal laminar surface, and 6) invasion into the cardiac cushion. Results of a three dimensional type I collagen gel culture model used to study EMT suggest that the presence of myocardium and endocardium solely in the AV canal and OFT are competent to undergo EMT. By HH20, numerous mesenchymal cells are observable in the two endocardial cushion-forming areas (Figure 2.5).

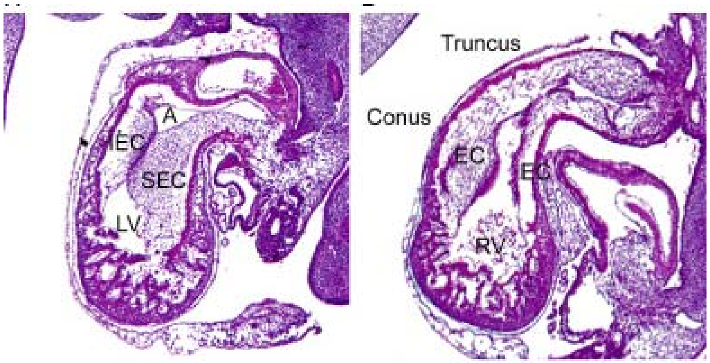

Figure 2.5 Cross-sectional image of endocardial cushion in HH20. A, atrium; IEC, inferior endocardial cushion; SEC, superior endocardial cushion; EC, endocardial cushion; RV, right ventricle. Image adapted from [32] with permission from Elsevier, copyright 2005.

The position and morphology of the AV canal and OFT are also experiencing dramatic changes during the time of endocardial cushion formation and EMT. In Figure 2.6, the AV canal undergoes a ventral and caudal displacement with respect to the common atrium and systemic venous sinus, and a leftward shift with respect to midline of embryo. Most importantly, the AV canal, together with the primitive ventricle, rotates ~90 degree counterclockwise along its original cranio-caudal axis[5]. This rotation causes the previous ventral and dorsal endocardial cushions to become superior and inferior endocardial cushions, respectively (Figure 2.6 A and C). This rotation of the AV canal is significant because the alignment of future tricuspid (separate right atrium and ventricle) and mitral valves (separate left atrium and ventricle) shifts from the original (before looping) dorso-ventral axis to the left-right axis (during early S-looping) that resembles a mature heart[5].

Changes are more complicated in the OFT. As it continues to elongate throughout looping phases, it is divided into the proximal portion (conus) that connect with right

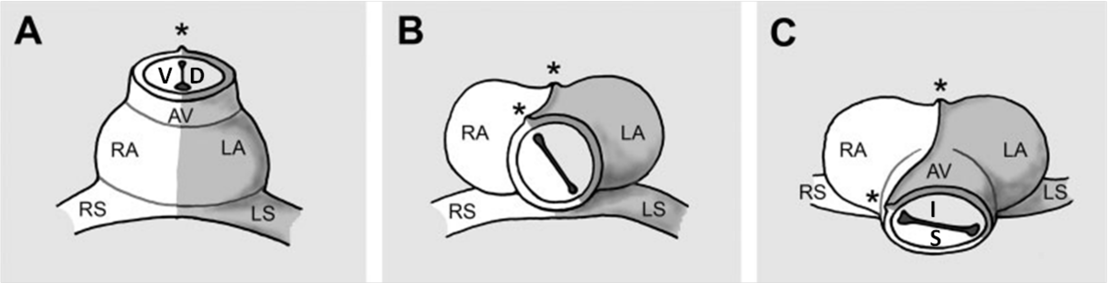

Figure 2.6 Schematic drawing of AV canal rotation. V, ventral side; D, dorsal side; RA, right atrium; RS, right horn of the systemic venous sinus; LA, left atrium; LS, left horn of the systemic venous sinus; I, inferior side; S, superior side. Image adapted from [5] with permission from John Wiley and Sons, copyright 2008.

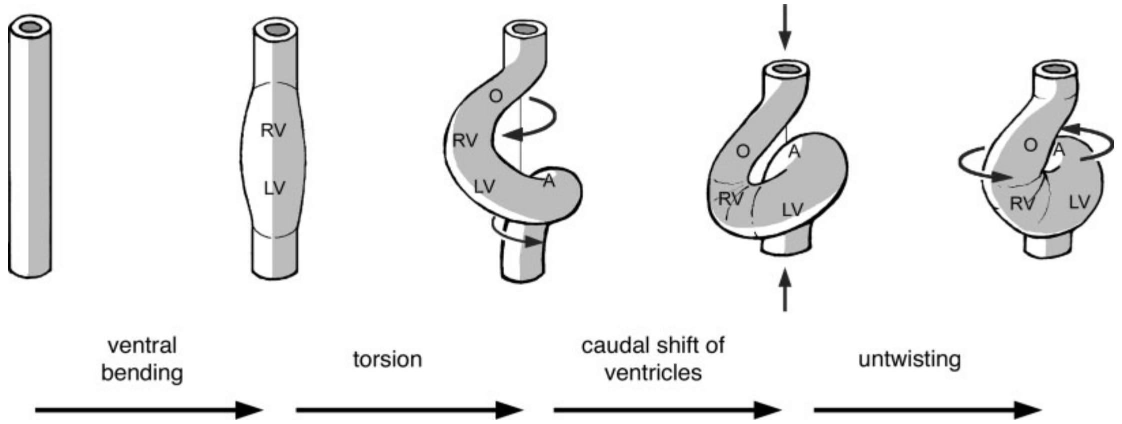

Figure 2.7 Schematic overview of location and morphological changes of ECH during looping phases. RV, embryonic right ventricle; LV, embryonic left ventricle; O, outflow tract; A, common atrium. Image adapted from [5] with permission from John Wiley and Sons, copyright 2008.

ventricle and the distal portion (truncus) that connect with the aortic sac at the dorsal midline. The conus follows the positional and morphological changes of the right ventricle. The torsion and caudal shift of the right ventricle cause a rightward displacement and a rightward tilt of the longitudinal axis with respect to the center line of the ECH. It should be noted that the torsion of the right ventricle causes an angular shift of the orientation of conus (Figure 2.7) along with endocardial cushion inside. Therefore, the previous left and right walls become ventral and dorsal walls, respectively, and the endocardial cushion becomes parallel with AV canal at this time point. Although the truncus is thought to be fixed in position, it actually comprises neural crest cells, which originate from the neural tube and migrate through pharyngeal arches 3, 4, and 6 [35], continuously adding to the neural tube's cranial end at the late S-looping phase. In contrast to the conus, the truncus experiences neither a location shift nor an orientation shift. As a consequence, the cardiac walls and endocardial cushions in the truncus remain in their original positions before looping with respect to the L-R axis throughout the EMT [36].

After the endocardial cushions are populated with mesenchymal cells, a series of differentiation events occurring in the AV canal and OFT lead to the maturation of valvular and septal structures[37]. The inferior and superior endocardial cushions in the AV canal continue to expand and eventually fuse to separate the AV junction into left and right orifices (HH26) [32]. Then, the AV canal shifts rightward to line up with the developing ventricular septum (Figure 2.8B). The fused inferior and superior cushions, now the AV septum, experience further remodeling to form posteroinferior and septal leaflets of the tricuspid valve and the aortic leaflet of the mitral valve (Figure 2.8 C and D) [32]. Simultaneously, the endocardial cushions to the left and right side of the AV canal are responsible for the lateral side of the newly formed AV junction [32].

In the OFT, endocardial cushions in inferior and superior positions also fuse to form the aorticopulmonary septum, which separates the truncus into the aorta and the pulmonary arteries (Figure 2.9 C and D). Figure 2.9 compares endocardial cushion position and morphology at the AV canal and the OFT and their corresponding fates.

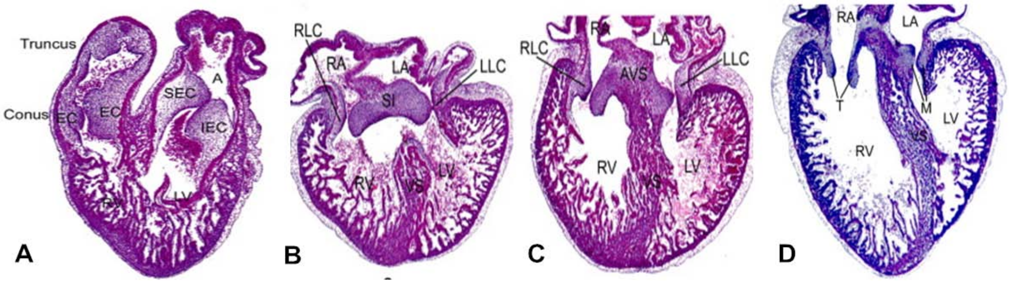

Figure 2.8 Endocardial cushion remodeling into mature heart valve and septa. EC, endocardial cushion; RV, right ventricle; LV, left ventricle; SEC, superior endocardial cushion; IEC, inferior endocardial cushion; RLC, right lateral cushion; SI, septum intermedium; VS, ventricular septum; LLC, left lateral cushion; AVS, atrioventricular septum. Image adapted from [32] with permission from Elsevier, copyright 2005.

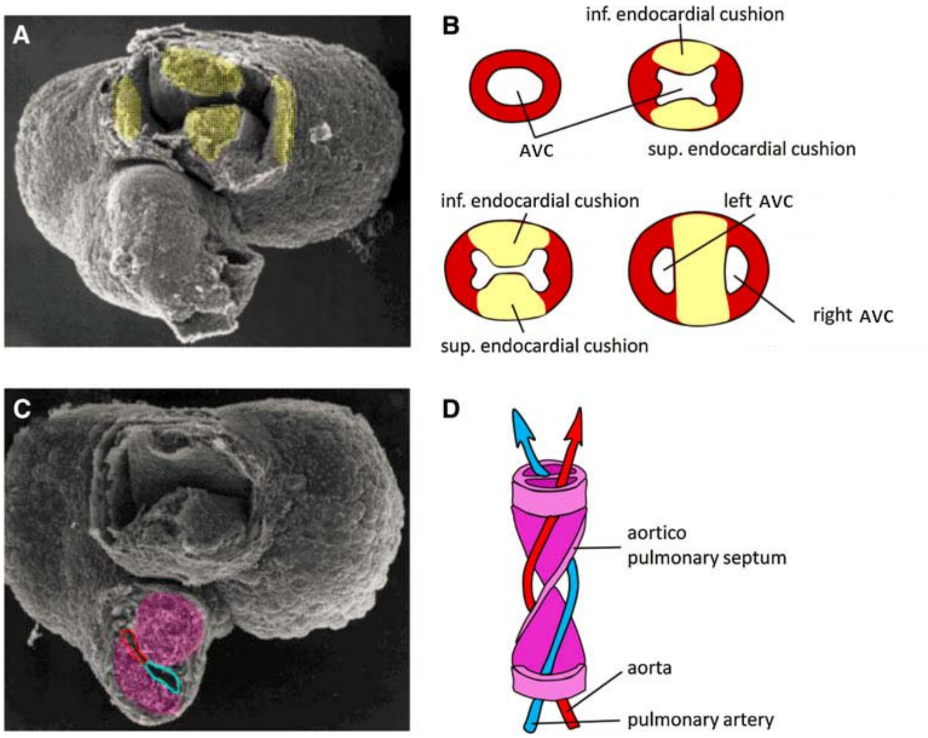

Figure 2.9 SEM images of AVC and OFT and schematic diagrams of cushion development. Image adapted from [38] with permission from Springer, copyright 2011.

2.2 **Fluid dynamics of embryonic heart**

The ECH valve and septum malformation mechanisms are currently poorly understood, but they are believed to result from interaction between genetic and environmental factors. For example, in the section 1.2 , we proposed that shear stress alteration could cause failure of endocardial cushion formation, which eventually causes congenital valvular and septal malformation. Since section 2.1 described the genetic process of embryonic valve and septal formation, this section will explain the effect of dynamic flow on morphologic remodeling.

Fluid shear stress is a frictional force of blood flow parallel to blood vessels walls and follows the direction of the flow. Shear stress has been proven to be regionally regulated in the embryonic heart lumen, where high shear stress is found only in the AV canal and the OFT; low shear stress is present in the remaining areas. Notably, this distribution of high shear stress overlaps distribution of primary cilia. Poelmanns'group [15] showed in field emission SEM images that a) primary cilia expression on the endocardial surface of the AV canal and OFT was significantly fewer than that on embryonic ventricular endocardial surface, b) the lumenal surface of the inner curvature of the AV canal, which experiences more shear stress than the outer curvature, was smoother than the remaining lumenal surface in the AV canal, and c) over time, when then enlarged chambers experienced less shear stress than during early stages, the primary cilia increased in number and length.

Although the mechanism underlying this phenomenon is unknown, it has been proposed by Hierck's group that primary cilia act as the mechanosensing organelle and respond to shear stress by expressing KLF2 and KLF4, which promote the EMT process in the embryonic heart [11]. Their study confirmed that a) shear stress-induced EMT took place only in nonciliated epithelial cells (EC), b) primary cilia amplified cytoskeletal strain, leading to prolonged gene expression of KLF2 and KLF4, c) overexpression of KLF4 prevented shear-induced EMT, and d) rescue of primary cilia prevented shear-induced transdifferentiation.

Based on the above results, we hypothesize that when a previously high shear stress area (cushion-forming area) is manually altered into a low shear stress area, the EMT process will fail, ultimately causing congenital heart valve and septal malformation.

To test primary cilia-mediated mechanotransduction, one must understand the profile of blood flow in the embryonic microcirculation environment. Here, we briefly review the fluidic dynamic parameters in ECH.

Currently most studies evaluate embryonic blood flow as a Newtonian fluid that can be described by the Navier-Stroke equation:

$$\mathrm{Re}=\frac{\rho UL}{\mu} \qquad \text{Eq 2-1}$$

Where Re is the Reynolds number that can be considered as the ratio of inertial forces to viscous forces, ρ is the density of flow, U is the characteristic velocity (i.e., peak velocity), L is the characteristic length scale (i.e., diameter of vessel), and μ is the viscosity [39]. By definition, the Reynolds number Re>>1 when inertial flow is dominant (e.g., the flow-transmitting aortic valve) and Re<<1 when viscous flow is dominant. Embryonic blood flow is typical viscous force dominant flow with Re value at about 0.02 when the embryonic heart first forms. It should be noted that due to the small diameter of the embryonic heart tube and cell interaction with tube walls, there is an alteration in shear rate and viscosity, which causes non-Newtonian effect. However, since red blood cells make up only 10-15% of the volume of the embryonic heart, this non-Newtonian effect is negligible.

In this paper, the periodic pumping mechanism of flow is considered as peristalsis because temporally, the period to be examined is before valve formation; spatially, the lumens of the AV canal and OFT can be evaluated as a short straight tube with axially symmetric structure [40]. With this in mind, the shear stress can be described as:

$$\tau_w = -\frac{32\mu Q}{\pi D^3} \qquad \text{Eq 2-2}$$

Where Q is the volumetric flow rate and D is the diameter of the blood vessel. From this equation, shear stress is linearly related to flow rate, with the proportionality constant μ. This equation is true under the assumption that the embryonic heart to be examined is a circular cylinder, and the blood flow is incompressible with uniform density and viscosity. Therefore the shear stress is proportional to velocity value.

To quantify the unsteady effects of pulsatile flow, the Womersley number (Wo) is useful:

$$Wo=L\sqrt{\frac{\omega\rho}{\mu}} \qquad \text{Eq 2-3}$$

where ω is the angular frequency of the pulse. If Wo value is high, then the velocity is highest near the midline of vessel and drops to zero at the vessel wall. Otherwise, if Wo value is low, the velocity profile over a cross-section of the vessel is parabolic, and the flow is quasi-steady and viscous-dominated. During the early developmental stages of ECH that concern us, the diameter of the tube is ~50 μm, the heart beats at ~2 Hz with peak flow rate at ~1 mm/s, the blood flow density is ~1.025 g/cm^3, and viscosity is set at 0.03. That yields a Wo value of 0.11, which agrees with the conclusion that when the Wo value is low, the flow is viscous-dominated.

In summary, blood flow at early embryonic developmental stages is at the rate of approximately 1 mm/s and linearly related with shear stress via viscosity. The flow can be evaluated as viscous dominate flow, and the shear profile is expected to be parabolic at the plane of cross-section along the direction of flow.

2.3 **Fourier domain OCT (FDOCT), OCM, and Doppler OCT**

FDOCT is a fast noninvasive cross-sectional imaging technique widely used for research and clinical purposes in areas such as ophthalmology, cardiology, and oncology.

In this section, the key parameters of FDOCT will be explicitly explained. And OCM and Doppler OCT (DOCT), which can be conceived as functional derivation of FDOCT, will be reviewed.

Conventional time domain OCT (TDOCT) [41] uses low-coherence interferometry to produce signals scattered from two optical paths in a way that is analogous to ultrasound imaging. In low-coherence interferometry, light reflected from imaging an object containing time-of-flight information including the reflective boundaries’ location and intensity interferes with light reflected from the reference mirror when the two beams transmitting same optical path lengths. By scanning the reference mirror in the longitudinal axis, the delay information can be used to determine reflection site and reflective intensity in the longitudinal direction of the imaging object. This imaging mechanism is analogous to ultrasonic pulse-echo imaging [41].

FDOCT [42] stands out in the field of optical imaging because it needs no scanning motion of a reference mirror as TDOCT does. Thus, the imaging speed of a longitudinal scan (A-scan) is enhanced. In FDOCT, instead of reference mirror movement in the longitudinal (axial) direction, the light reflected from the sample containing information of all reflective layers along the axial direction in the sample is recombined with light reflected from the fixed-position reference mirror. The recombined light is spatially split into a chromatic spectrum by a refractive grating, and a spectrometer records the spectrum.

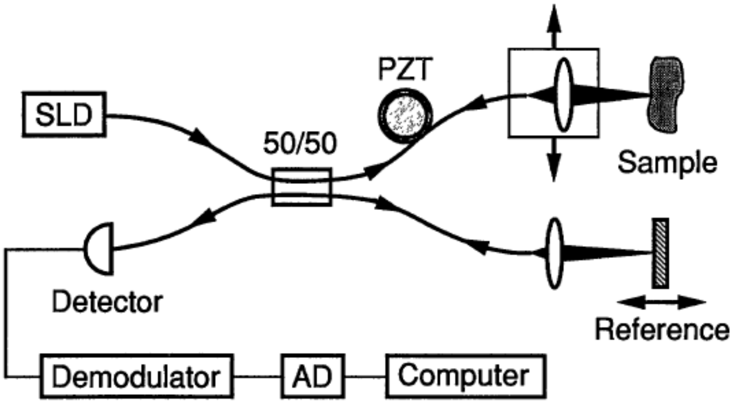

Figure 2.10 Schematic of TDOCT imaging set up. SLD, superluminecent diode; PZT, piezoelectric transducer; AD, analog to digital conversion. Image adapted from [41] with permission from Science, copyright 1991.

This wavelength-dependent intensity spectrum contains the information of all reflective layers in the sample in the axial direction at one lateral location. Therefore, by one single exposure of the spectrum, one line of reflective layer information, instead of one point, is obtained.

Unlike TDOCT, the imaging mechanism of FDOCT is explainable only by mathematical deductions. In Figure 2.10, the interferometer in OCT evenly divides a broadband source field $E_i(\omega)=A_i*e^{i\omega t}$ into reference field E_r and sample field E_s with $E_r(\omega)= E_s(\omega)=1/\sqrt{2}A_i * e^{i\omega t}$, where A_i and ω are the field's amplitude and angular frequency, respectively. Although the light reflected from the reference mirror has no phase alteration in the optical field, light reflected from the sample is modified as:

$$E_s(\omega)'=\int 1/\sqrt{2}A_i r(z)^* e^{i(4\pi\frac{n(\upsilon)\upsilon}{c}z+\omega t)}\,dz \qquad \text{Eq 2-4}$$

where z is the distance offset in the longitudinal direction in the sample in comparison with the reference arm, r(z) is the reflection coefficient as a function of z, υ is the frequency of the field, and $n(\upsilon)$ is the refractive index of the sample medium as a function of υ.

The two reflected lights recombine at the detection arm, where the light is sensed by the detector as an intensity term (angular brackets denote integration over the response time of the detector):

$$\begin{aligned} I(\omega)' &= \frac{1}{2}\langle (E_r+E_s{}')(E_r+E_s{}')^*\rangle \\ &= \frac{1}{2}\langle E_rE_r{}^* + E_s{}'E_s{}'^*\rangle + Re(E_r{}^*E_s{}') \\ &= \frac{1}{4}A_i{}^2 + \frac{1}{4}A_i{}^2\int r^2(z)dz + \frac{1}{2}A_i{}^2\int r(z)e^{i4\pi\frac{n(\upsilon)\upsilon}{c}z}dz \qquad \text{Eq 2-5} \end{aligned}$$

where the first term is the direct current (mean intensity) signal originating directly from the light source, and the second constant term, the source intensity, is modulated by integration of the reflection coefficient, which is negligible. The third term, which contains the reflection coefficient information of the sample, is written in the form of a Fourier transform:

$$\begin{aligned} \frac{1}{2}A_i{}^2\int r(z)e^{i4\pi\frac{n(\upsilon)\upsilon}{c}z}dz &= \frac{1}{2}A_i{}^2 FT(r(\frac{2n(\upsilon)\upsilon}{c})) \\ &= \frac{1}{2}A_i{}^2 FT\left(r\left(\frac{2}{\lambda}\right)\right) = \frac{1}{2}A_i{}^2 FT\big(r(k)\big) \qquad \text{Eq 2-6} \end{aligned}$$

where FT represents the Fourier transform, λ is the wavelength of the spectrum, and k is the wave number. Therefore, the signal the detector acquired is a constant plus the Fourier transform of the reflection coefficient as a function of wave number, which represents the location and intensity information of all layers within penetration in the sample.

From Eq 2-5 and Eq 2-6, the data processing to obtain spatial information of the sample is as follows: 1) record and subtract the light source spectrum to delete the DC term of the signal, 2) convert the spectrum so that it is evenly distributed from λ domain to k domain, 3) perform a Fourier transform of the preprocessed signal. These are the basic data processing to obtain spatial information.

When evaluating an FDOCT image, there are several key parameters to be considered. First is the axial resolution of a Gaussian beam given by [43]:

$$l_c = \frac{2\sqrt{\ln 2}}{\pi} \frac{{\lambda_0}^2}{\Delta\lambda} \qquad \text{Eq 2-7}$$

where λ_0 is the center wavelength of the light source, and $\Delta\lambda$ is the bandwidth of the light source. From Eq 2-7 it can be seen that the axial resolution is solely dependent on the parameters of the light source: the shorter the center wavelength and the wider the spectrum, the better the axial resolution.

The second important parameter is sensitivity. This parameter of OCT is represented by the highest possible attenuation in the sample arm that still allows the sample to be detected, at which the signal to noise ratio (SNR) equals 1 [44]. In FDOCT, sensitivity is measured in decibels, and the higher the value, the better the performance of the system. Shot noise caused by the light from the reference arm is the main noise that limits sensitivity of FDOCT, and the expression of shot noise-limited sensitivity is given by [43]:

$$SNR=\frac{\rho S(k)R}{4eB}M \qquad \text{Eq 2-8}$$

Where ρ is the responsivity of the detector, S(k) is the intensity spectrum received by the detector, R is the power reflection coefficient that equals the squared integral of r(z) over penetration depth, e is the electronic charge of the detector, B is the electronic bandwidth of the detector, and M is the sampling number (i.e., pixel number of the detector). Therefore, besides the performance of the detector, increasing light source intensity and number of sampling is useful in improving the sensitivity of OCT system.

Another key factor in evaluating OCT imaging is the imaging depth. This parameter is inversely proportional to the spectral sampling resolution $\delta_s k$. The total wave number range Δk is the product of spectral sampling resolution and sample number M. Therefore the imaging depth of a FDOCT image is given by:

$$z_{max}=\frac{\pi}{2\delta_s k} \qquad \text{Eq 2-9}$$

From Eq 2-9, it should be noted that imaging depth is limited because of finite sampling of the spectrum in the practical world, which also limits the acquisition of high frequency fringes in the spectrum, resulting in the phenomenon, sensitivity falloff.

Finally, lateral resolution also accounts for how clearly an object is displayed, especially when stacking B-scans together and examining the en-face image after 3D reconstruction of OCT cross-sectional images. The lateral resolution of OCT is limited exclusively by diffraction limit of the focusing optics, which could be either a lens or a microscopic objective:

$$\delta_x=0.37\frac{\lambda_0}{NA} \qquad \text{Eq 2-10}$$

where NA is the numerical aperture of focusing optics. When applying an objective as the focusing optics, the OCT system is termed OCM because rather than generating a cross-sectional image as in OCT, OCM illustrates the en face images resembling the features of microscopic systems due to limitation of depth of field (Figure 2.11). With the combination of high numerical aperture in the lateral direction and coherence gating in the axial direction, OCM enables cellular level imaging without sacrifice of animal model and staining of the live tissue, which is required in conventional microscopic imaging techniques. Furthermore, OCM demands lower numerical aperture focusing optics when providing the same lateral resolution and yet provides greater depth of detection than confocal microscopy.

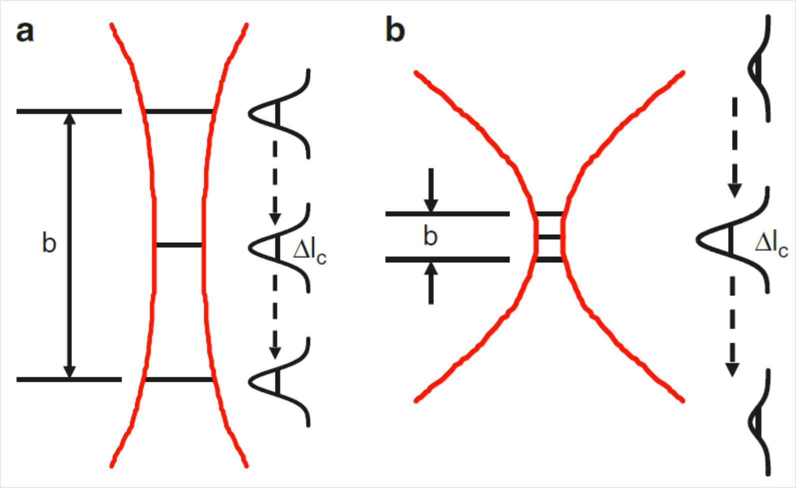

Figure 2.11 Comparison of depth of field in OCT and OCM. b, depth of filed, Δl_c, coherence length. Image adapted from [45] with permission from Springer, copyright 2015.

Besides OCM, FDOCT has another important functional extension, Doppler OCT, to simultaneously image internal structure and quantitatively measure flow profile in highly scattering media. The imaging mechanism of Doppler OCT is to combine Doppler flowmetry with FDOCT as follows: The Doppler Effect is the frequency shift of a detected wave (e.g., light) from a source that is moving relative to the detector, and the frequency shift is given by the following equation:

$$f_d = \sqrt{\frac{c+v}{c-v}} f_0 \qquad \text{Eq 2-11}$$

where f_d represents the Doppler-shifted frequency, f_0 is the original frequency of the light, c is the velocity of the light, and v is the relative moving velocity between the source and the detector. By measuring the shifted frequency, the velocity can be obtained.

In practical implementation, as shown in Figure 5, the particle seeded into the flow (e.g., a blood cell in the blood flow) as a moving detector will interact with the illumination light, the frequency of which will be Doppler-shifted relative to that of the original light from the source, and the light scattered by the moving particle will experience frequency shift again when it is measured by the stationary optical detector. If the particle is moving at the velocity of u, and c is much larger than u, we have:

$$\Delta f = f_d - f_0 = \frac{2u\cos\theta}{c} f_0 \qquad \text{Eq 2-12}$$

Where u is the velocity of the blood cell and the sample arm of the OCT forms an angle of θ with the direction of flow as shown in Figure 2.12.

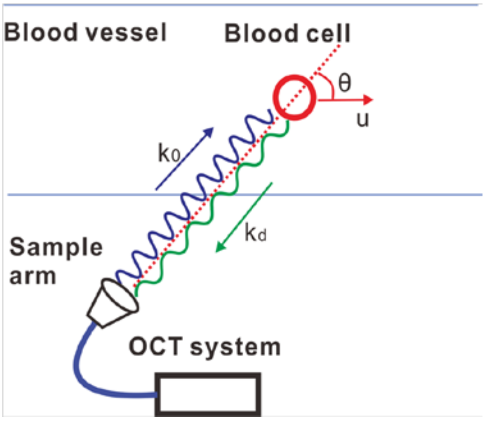

Figure 2.12 Schematic of Doppler OCT imaging mechanism.

Therefore, the flow velocity is determined by the Doppler shift and the angle formed by the sample beam and the flow direction [46]. The Doppler shift can be obtained by analyzing the phase term in FD-OCT [27, 46]. This approach, phase-resolved OCT, maintains high imaging speed while attaining blood velocity with high spatial resolution and sensitivity. However the result is inaccurate due to 1) phase analysis that provides Doppler velocity signals, but adds intrinsic noise in comparison with intensity analysis, which provides only morphological information, and 2) difficulty in determining Doppler angle since the imaging objects usually do not present well defined outlines that make it feasible to orient with the sample arm.

In conclusion, FDOCT provides a fast, noninvasive approach to obtain cross-sectional images of live tissue with cellular level resolution and milliliter level penetration. The functional extension of FDOCT, OCM and Doppler OCT, are able to produce high lateral resolution and velocity measure respectively besides the properties inherent from FDOCT.

2.4 **PIV imaging**

PIV gives instantaneous velocity measurement by calculating the particle displacement in consecutive images on a single plane. The imaging setup of conventional PIV usually consists of the following parts as shown in [47]: small tracer particles injected in the tunnel travel along with the flow and are illuminated by a light sheet generated from a laser source and optical systems; light scatted from the tracer particles is detected and recorded on camera via imaging optics placed in a direction perpendicular to

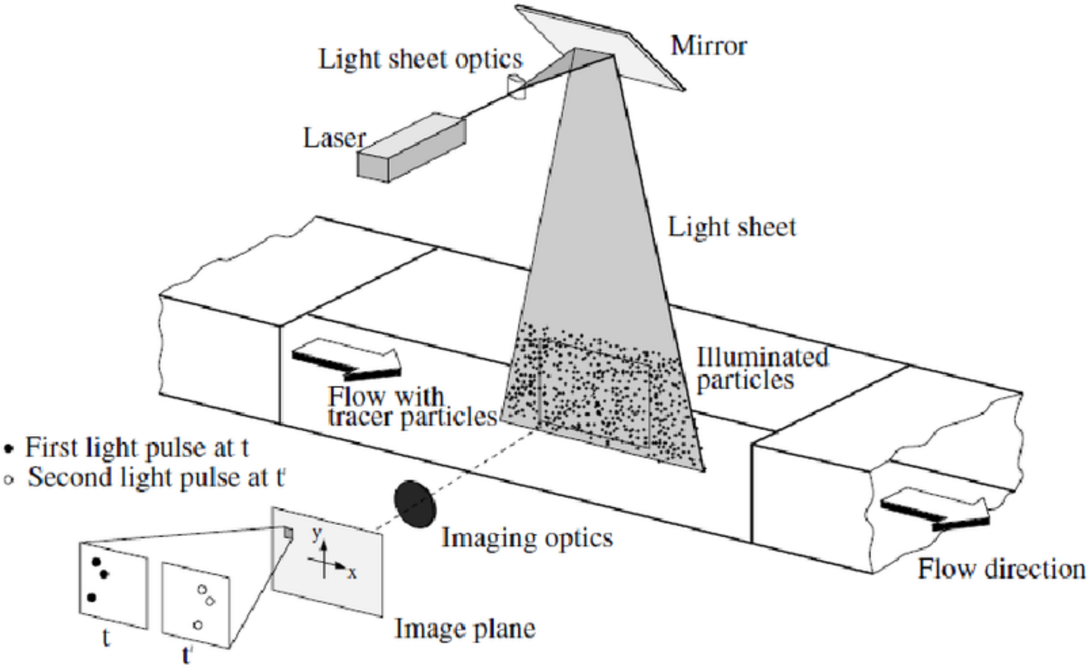

Figure 2.13 Diagraph of conventional PIV set up. Image adapted from [47] with permission from Springer, copyright 2007.

the light sheet; the laser source should be able to pulse at least twice to expose tracer particles onto digital recorders within a short time interval to provide useful PIV raw data; the digitalized data is transferred to computer memory; in the computer, one frame of PIV raw data is divided into small subareas termed interrogation spots and auto/crosscorrelation of corresponding interrogation spots in two consecutive images are performed to determine local displacement vectors; local flow velocity vectors are calculated, taking into account the time interval of consecutive images and magnification at imaging (Figure 2.13).

The PIV setup for microfluidic quantifications (μPIV) [48] is conducted on microscopy basements; the main differences from conventional PIV are shown in Figure 2.14. Instead of the illuminating light sheet, μPIV applies illuminating light shooting on fluid flow via a microscopic objective to resolve micrometer-level fluorescent tracer particles.

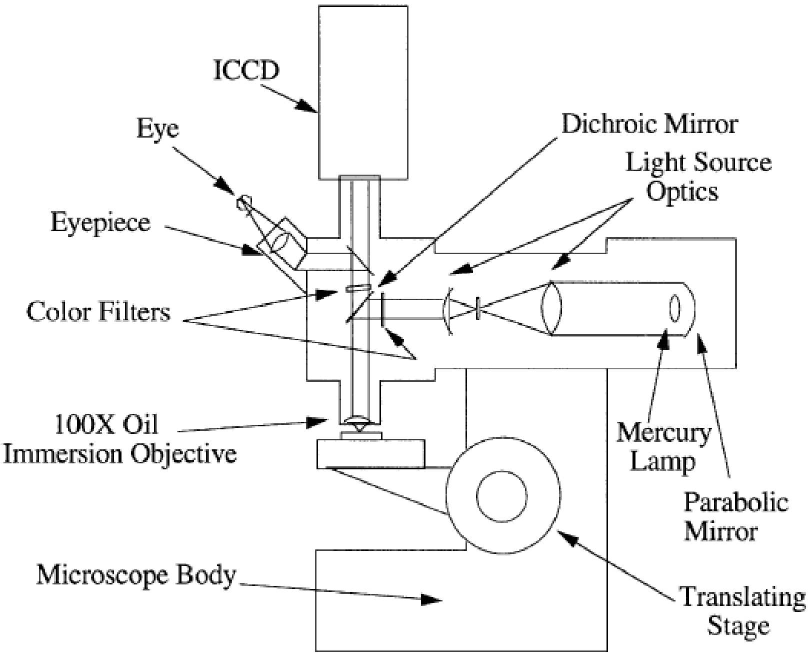

Figure 2.14 Diagraph of μPIV setup. Image adapted from [48] with permission from Springer, copyright 1998.

The emitted fluorescent light from tracer particles follows the light path overlapping with the illuminating light until they are split by the dichroic mirror. Then the fluorescent light is divided again by a beam splitter for the purpose of observation via eyepiece and recording via camera. The objective is normally of high numerical aperture to create a thin layer of depth-of-field that resembles the properties of the illuminating light sheet in conventional PIV.

Of several key factors in μPIV,, first is the postacquisition data processing that calculates the velocity vectors. For this process, one can choose to first have the camera double-expose two consecutive images on one frame and or single-expose the two images to separate frames and then, respectively perform autocorrelation or crosscorrelation to calculate the interrogation displacement. Crosscorrelation has replaced autocorrelation [49] as the algorithm to determine displacement of the interrogation spot because 1) crosscorrelation can solve the direction ambiguity problem that happens in autocorrelation, 2) crosscorrelation is able to resolve the zero displacement, which is embedded in the self correlation peak in autocorrelation, 3) crosscorrelation provides better SNR than autocorrelation due to decreased exposure time. The result of using autocorrelation and crosscorrelation on the same velocity field are shown in Figure 2.15, and the advantages of crosscorrelation over autocorrelation are clearly exhibited.

Since the interrogation spot acts as the unit for postacquisition data processing, determining the spot size is crucial for PIV result [50]: 1) the interrogation spot size should be small enough to maintain the resolution of the resulting velocity map; 2) since

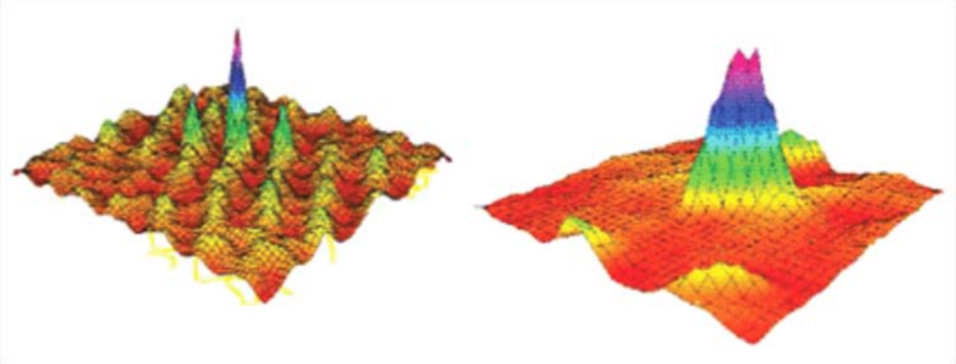

Figure 2.15 Comparison of autocorrelation and crosscorrelation result based on calculation of the same flow field [51]. Image was reused with the permission from author.

the maximum displacement obtainable is half the size of the interrogation spot (from the correlation process described above),, the spot size should be at least twice the estimated displacement during double exposures; 3) the spot should contain at least 5-10 particles to keep the correlation result genuine; 4) the spot should be sufficiently large so that particle moves less than one-fourth of the size of the spot to elevate SNR. With these requirements, the spot size is given by:

$$d \geq 4m\Delta tu \qquad \text{Eq 2-13}$$

where d is the side length of the square interrogation spot, m is the recording magnification, and Δt is the time interval between adjacent exposure.

Another important factor is the choice of tracer particles that travel within flow. The tracer particle should 1) follow and represent the flow behavior without excessive slip caused by gravity and 2) scatter sufficient light for the recording device [50]. Therefore the diameter and density of tracer particles require careful consideration in the context of fluid flow. A simple way to evaluate a tracer particle is under the assumption of Strokes drag:

$$u_s = \frac{g d_p^2 (\rho_p - \rho_f)}{18\mu} \qquad \text{Eq 2-14}$$

where u_s is the settling velocity in the opposite direction of gravity, g is the acceleration due to gravity, d_p and ρ_p are the diameter and density, respectively, of the tracer particle and ρ_f and μ are the density and viscosity, respectively, of fluid flow. Particles are considered suitable when u_s is negligible compared to the travel velocity of the tracer particle.

CHAPTER 3 DEVELOPMENT OF THE OCM SYSTEM WITH A BESSEL ILLUMINATION BEAM

3.1 **Introduction**

Because of their three dimensional high resolutions and non-invasive imaging properties, OCM systems have been used to define the morphology of cellular-level structures in vivo and in situ [52-55]. The *en-face* image of blood cells flowing inside a vessel was illustrated by an OCM setup with a speed of 4 frames/s[52]. Although the short coherence gate that results from broadened the spectrum of the light source provides better sectioning performance when taking en-face images compared with a confocal gate, it retains the depth information along the incident axis. This property of OCM is inherited from OCT, which provides the possibility of using OCM to perform PIV imaging. Another advantage of OCM in the application of measuring blood flow is that the illumination light, which is of milliwatt-level power, is always infra light at either the 800nm or 1300nm range, making it feasible to penetrate tissue with noninvasive and nontoxic effects for a protracted period of time.

Chen’s group has demonstrated improved focusing range, or depth of focus, by replacing the conventional focusing lens in an OCT system with axicon lens at the sample arm. As a result, the OCT system extended its focusing range to 6 mm, in comparison with the Rayleigh range (less than 0.25 mm) for a Gaussian beam with the same resolution [56].

Bessel illumination refers to the intensity distribution of a beam follows the Bessel function of first kind, whose cross section is a set of concentric rings. Practically, Bessel illumination is always created by an axicon lens. Bessel illumination can also be incorporated into an OCM system by having the axicon lens act as a conjugate lens to the objective, resulting in a linear relationship between the focusing depths exiting the axicon lens and the objective[57]. The advantage of utilizing Bessel illumination is not only to extend the focusing range of OCM system, but also to adjust the focusing range to the desired values by changing the parameters of the optical lens placed after the axicon.

In summary, the OCM system illuminated with a Bessel beam is capable of cellular-level imaging in the range of depth that is required for PIV imaging. But the optical system designs in the literature are suitable only for imaging stationary structures by scanning the sample stage. Therefore, a modification of OCM optical design is need to realize a fast B scan that is capable of measuring blood flow with maintained cellular level resolution over several hundred micrometers of depth.

3.2 **Materials and Methods**

Broadband spectrum generation

The imaging mechanism of OCM makes the axial resolution dependent only on the bandwidth of the light source spectrum once the center wavelength is determined. The axial resolution of an OCM system with Gaussian illumination is given by Eq 2-7, where $\Delta\lambda$ can be conveniently calculated as the full width half maximum (FWHM) of the intensity distribution of spectrum. Therefore, expanding the bandwidth of the spectrum enhances axial resolution. Application of photonic crystal fiber (PCF), which has been widely reported in OCT [58-60], expands the spectrum from visible to the near infrared by use of low-energy femtosecond pulses undergoing extreme nonlinear spectral broadening. In our system, the PCF we chose was the Newport SCG-800 Supercontinuum Fiber Module [61]. It is a pre-assembled device consisting of a polarization maintained core PCF sealed within a one inch diameter exterior package (the black tube shown in Figure 3.1) for ease of mounting. At both ends, the PCF is sealed and spliced with regular fiber, which requires an objective to either focus light for the purpose of coupling or collimate light that is emitted from the fiber end as a parallel beam.

To couple the laser beam into the PCF, the incident beam must be positioned close to the circular face of the PCF module to achieve high coupling efficiency. A pair of steering mirrors was used to achieve the normal position of the beam. A 4F system was applied immediately before the light entered into the coupling objective to expand the beam to the degree that fully exhibits the numerical aperture of the coupling objective. This process also assisted in elevating coupling efficiency since the focusing beam waist is minimized when the incident light covered the entire rear aperture of the objective, which facilitated the light entering the small pin hole on the end of the fiber. The coupling and collimating objectives were chosen to be 20X magnification according to manufacturer's recommendation [61] for the purpose of obtaining a stable supercontinuum with negligible minor incident beam misalignments.

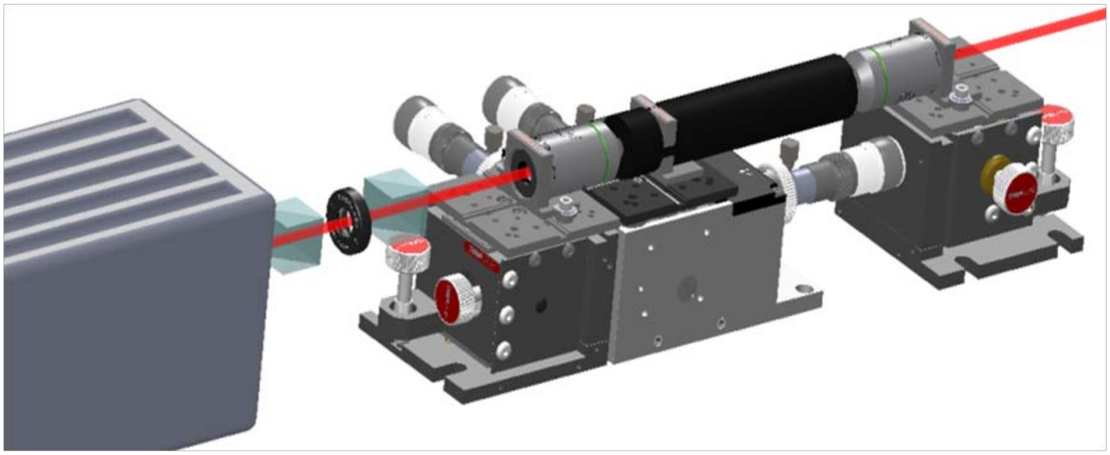

Figure 3.1 Drawing of experimental setup for coupling laser beam into PCF using differential stages and a pair of 20X objectives for focusing and collimating.

The differential coupling stage pair design was another important factor to achieve high coupling efficiency. The translation stage housing the PCF was Thorlabs MAX313D 3-Axis NanoMax Stage with a manual step size of 1 μm. The differential stage housing coupling objective was Thorlabs MBT602 3-Axis MicroBlock Stage with Thumbscrew Adjusters that allow 500 μm travel distance per revolution. The cooperation of the differential stage pair made it possible to adjust PCF in sub-micrometer steps with respect to the location of the objective.

Bessel illumination and characterization

Bessel illumination is the electromagnetic field whose intensity distribution on the cross-section is perpendicular to the propagation direction and follows the Bessel function of first kind. The field propagates and maintains its original distribution even with the presence of obstacles in the main lobe of the Bessel function [62, 63]. Because of these properties, Bessel illumination has been reported to exhibit better positional stability and beam quality than Gaussian beams when penetrating highly scattering tissues [64]. For these reasons, Bessel illumination has recently been investigated regarding the feasibility of improving the deep-tissue imaging performance of various microscopy techniques [65, 66]. Most of the time, an axicon lens with a particular top angle is applied to convert a Gaussian beam to a Bessel beam that directly illuminates the sample. Characterizing the

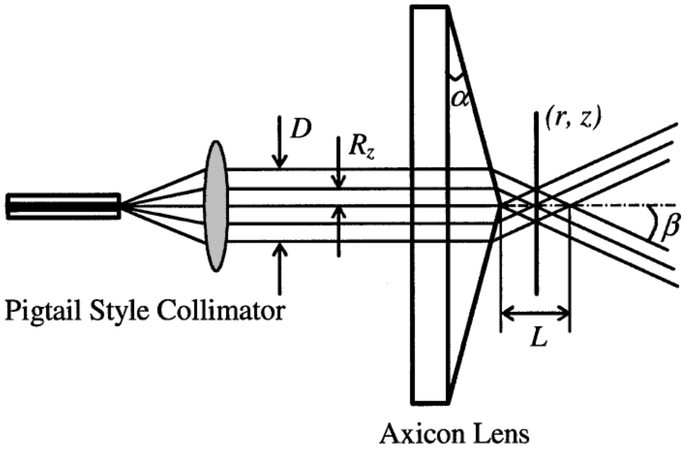

Figure 3.2 Schematic of axicon lens converting Gaussian beam into Bessel beam. Image adapted from [56] with permission from Optical Society of America, copyright 2002.

axicon-generated Bessel beam shown in Figure 3.2[56], the intensity distribution of light J(r, z) at the radial position r and axial position z in respect to the exit of the axicon is given by[56]:

$$I(r,\ z)=E^2(R_z)R_z\frac{2\pi k\sin\beta}{\cos^2\beta}J_0{}^2(kr\sin\beta),\ R_z\leq\frac{D}{2},\ z\leq L \qquad \text{Eq 3-1}$$

where $E^2(R_z)$ is the energy of incident light, R_z is the radius of the incident beam, β is the angle formed by the axicon-exiting ray and the optical axis, J_0, is a zero-order Bessel function of the first kind, D is the beam diameter, and L is the depth of focus of the Bessel illumination. Based on Eq 3-1, the lateral resolution of Bessel illumination can be obtained by set $J_0=0$, and thereby we have the lateral resolution (ρ_0) expression:

$$\rho_0=\frac{2.4048}{k\sin\beta} \qquad \text{Eq 3-2}$$

From geometry, the depth of focus L can be approximated by:

$$L=\frac{D(\tan^{-1}\beta-\tan\alpha)}{2} \qquad \text{Eq 3-3}$$

where α is the angle formed by the conical and flat planes of the axicon.

However, to retain the high lateral resolution of our system, a beam focused by an axicon is insufficient for cellular imaging. Consequently, we placed the axicon lens in combination with an objective to enhance light focusing on the sample. Accordingly, we designed the Bessel illumination for both the sample and reference arms that was applicable in the OCM set up as the sample arm alignment shown in Figure 3.3. In our design, the incident Gaussian beam was transferred into the Bessel beam after a fused silica axicon (Thorlabs AX255B, n=1.46) with 170^{o} top angle. The optical axis of light was collimated with Lens 1 (F1=75 mm), and the beam ring was focused at the center of the scanning mirror. With Lens 2 and Lens 3, the optical axis of the beam was transferred parallel and the diameter of the beam was set to fit the rear aperture of the focusing objective (Olympus 10X UMPlanFL). The back focal plane of the objective was aligned at the conjugation plane with the center of the scanning mirror to ensure linear scanning and the rear aperture of the objective was close to the back focal plane so that every scanning beam was able to enter the aperture regardless of the scanning angle. Similarly, the objective was placed at the conjugate plane of the axicon so that the focusing range of the objective is linearly related to the focusing range created by the axicon. To maintain high axial resolution, dispersion mismatch is eliminated by having the reference arm designed to present the same set of optics as the sample arm except for the absence of the scanning mirror.

The advantage of our system in comparison with other applications of axicon in deep tissue imaging is that 1) the system required no scanning of sample stage because the scanner and back focal plane of the objective were placed at a pair of conjugation planes, which greatly elevated the scanning speed; 2) the focusing range starts apart from the exit of objective, making it easier in practice to perform imaging that requires a long working distance, and 3) the focusing range can be adjusted for different applications by changing

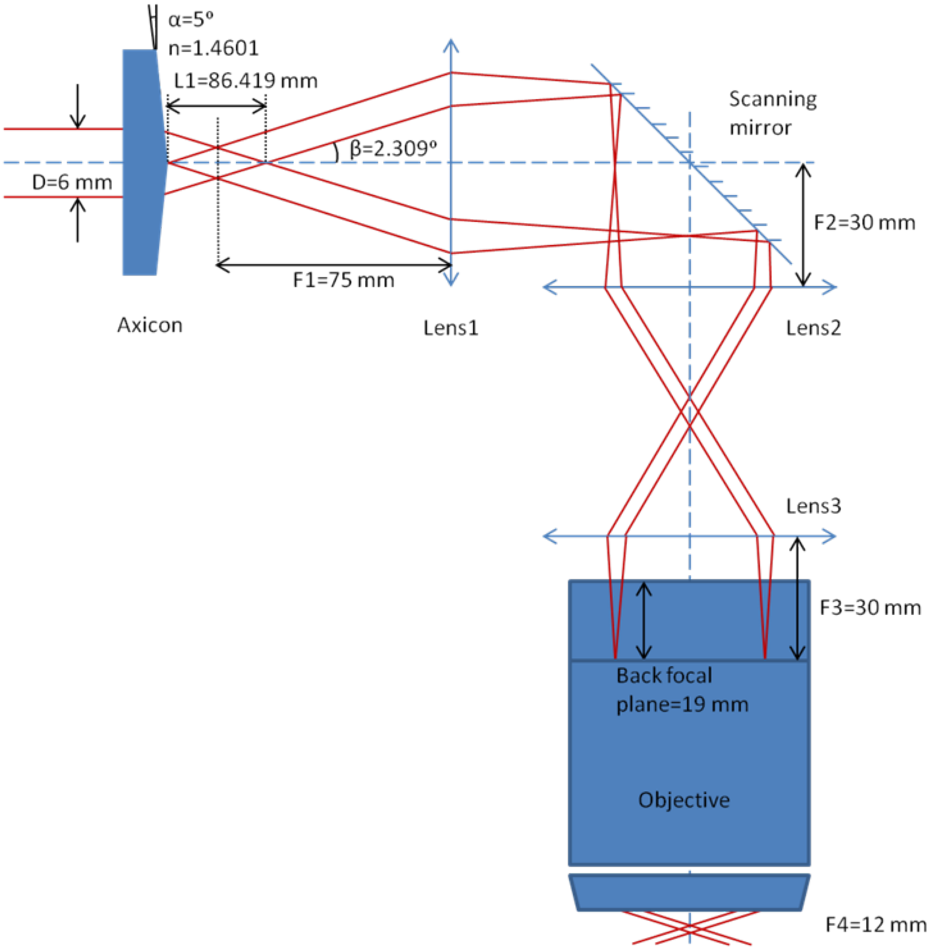

Figure 3.3 Schematic of Bessel illumination-incorporated OCM sample arm optical design

the parameters of the set of lenses placed ahead of the objective.

To demonstrate the optical field of Bessel illumination in comparison with conventional Gaussian illumination, we took sectional pictures of the distribution of the beam along the propagation direction to illustrate differences in the two distributions. The focusing range of Gaussian illumination is calculated by the expression [67]:

$$\mathrm{DOF}=\frac{25000\times\omega}{\mathrm{NA}\times\mathrm{M}}+\frac{\lambda}{\mathrm{NA}^2} \qquad \text{Eq 3-4}$$

where DOF represents depth of focus, another term of focusing range, ω is resolving power of eye (0.0014), NA is numerical aperture, M is total magnification, and λ is center wavelength.

Intensity distributions of both illuminations were also compared by manually scanning the optical axis of both beams and recording them with a camera (Carl Zeiss AxioCam MRm) with the same incident beam power. Intensity count was recorded as mean of 16 pixels with a step size of 100 μm, which was sufficiently small because the expected depth of focus of the Bessel beam is one to two millimeters.

Optical design of the Bessel illumination-incorporated OCM

The light source of the system was a Ti: sapphire femtosecond laser (Spectra Physics) with 80MHz repetition rate. The pumped light had a Gaussian spectral distribution centered at 830 nm with FWHM bandwidth of 20 nm. The incident beam $1/e^2$ diameter was expanded to 5 mm with a 4F system composed of two achromatic doublet lenses (F=15/75 mm). Then the light was coupled into the PCF as described above. The supercontinuum exiting the collimation objective was filtered (Thorlabs FEL0750 and FES0950) to obtain a 200 nm bandwidth spectrum centered at 850 nm. This broadband light was once again normalized with a pair of steering mirrors and collimated with a 4F

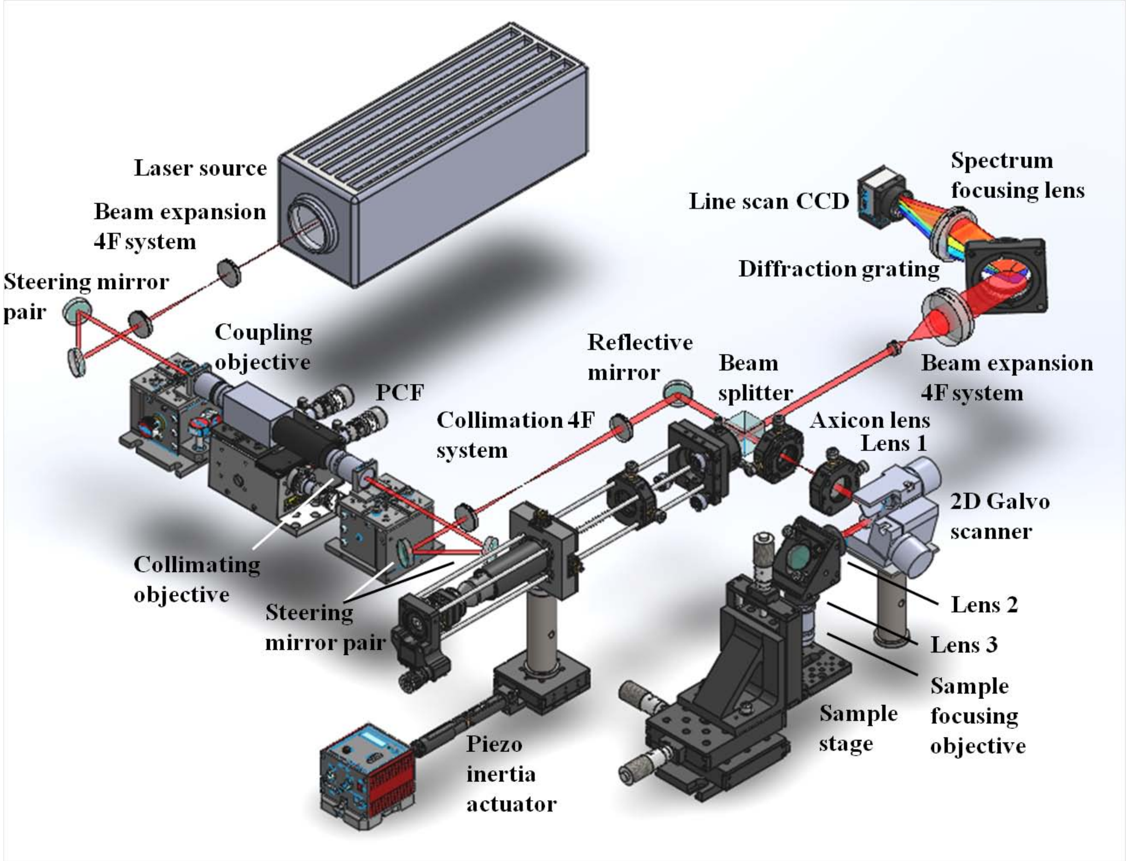

Figure 3.4 System set up using balanced optics in sample and reference arms.

system (F=50/50 mm) to achieve parallel beams before it was reflected onto beam splitter. The 50/50 beam splitter divided the incoming beam into two perpendicularly oriented parts that possessed the same power, the transmission part went to the sample arm, and the reflected part went to the reference arm. Light traveling in the two arms theoretically experienced the same diffraction procedures; at the ends of both arms light were focused by X10 Olympus objectives onto reflectors, which were a mirror in the reference arm and an imaging object in the sample arm. The beams reflected by the reflectors were captured by the objectives again and returned to the beam splitter via the previous optical paths.

The beams were recombined at the beam splitter and exited from the surface next to the light entrance surface. The beam was again expanded with a 4F system (F=30/75 mm) to cover about 1/3 of the area of the transmission diffraction grating (Wasatch Photonics 1800 lp/mm) for a good spectrum diffraction result. The diffracted spectrum was finally focused by an achromatic lens (F=150 mm) onto the line scan CCD (E2V AViiVA EM4). As a result, one A-scan of the OCM system corresponded to one line of the spectrum on the CCD. With one scan on sample (one B-scan), the CCD camera recorded 1000 lines as one frame. The CCD and scanner were synchronized to ensure each B-scan of the sample corresponded to one frame of the picture using a Labview coded external trigger program controlled National Instrumentation board. The board sent a trigger signal with 50kHz as the line rate of CCD, resulting in a 50 frame rate. While the X scanner was operating synchronously with the camera trigger, the Y scanner worked independently to scan in a perpendicular direction on sample with X scanner to achieve C scan.

Axial resolution characterization

The method we used to characterize axial resolution of the system was to place a silver reflective mirror at the end of the sample arm and observed the interference fringe at the detection arm [59]. The spectrum was adjusted to obtain a Gaussian-like shape that was convenient to quantify axial resolution. We scanned the entire reference arm in the axial direction with a motorized actuator (Thorlabs Z825B) mounted to the pedestal stage that holds the entire reference arm. The actuator could be computer controlled via a compatible motor drive (Thorlabs TDC001), which moved the pedestal stage at the speed of 20μm/s. Within the scanning range, the light reflected back from reference arm and sample arm interfered with each other, and the interference signal was coupled into a single mode fiber via collimator placed at the other side of diffraction grating. The light the collimator collected was zero order diffraction, which presented the same dispersion properties as the beam before diffraction. Therefore, the coupled light contained the same interferometric signal that exited the beam splitter. The interferometric signal was then transduced via an optoelectrical transducer and recorded as an intensity signal on an oscilloscope with sampling rate of 1GHz. The signal was then exported to Matlab on a PC to perform the plot function, and the resulting FWHM of the envelope of the plot is considered as the measured axial resolution of the system in air.

3.3 **Results**

The coupling efficiency of light entering into the PCF was 24.2% at room temperature, compared with an optimal efficiency of 30% as claimed by the manufacturer [61]. The coupled power was measured to be 230 mW, which was sufficient for our purpose of imaging fluid flow. The PCF expanded the original infra light into a supercontinuum with measurable bandwidth from 400nm to 1400nm. The supercontinuum was then filtered to obtain a bandwidth of 150 nm centered at 850 nm as the source for imaging.

Figure 3.5 is the spectrum intensity distribution results measured by an Ocean Optics spectrometer. The dotted line and solid line show the spectral intensity distribution of the laser before and after supercontinuum generation by the PCF, respectively. The PCF effectively expanded the spectrum 7.5 fold with a resulting power of ~100mW, which is sufficient for our purpose of imaging. This broadband spectrum distribution may differ slightly at times, but as long as the room temperature and humidity remained at a favorable level (20-22^{o}C, 28-32%), the spectrum was stable and its parameters, such as emitting power and bandwidth, remained the same value. Therefore, taking strict control of room temperature and humidity is fundamental for our experiments.

With a 150nm wide spectrum, the corresponding axial resolution is 2.13 μm in air according to Eq 2-7. To examine the axial resolution value, the reference arm was scanned to record the interferometric signal in an oscilloscope, and the result was shown below. During scanning, the piezo inertia actuator was externally controlled to move continuously at 20 μm/s speed, while the oscilloscope displayed each screen at 100 ms speed. The axial resolution was determined as FWHM of the envelope of the interferometric signal, which took 139 ms on the oscilloscope, resulting in a 2.78 μm axial resolution in air. The shape of the interferometric signal might differ at times due to

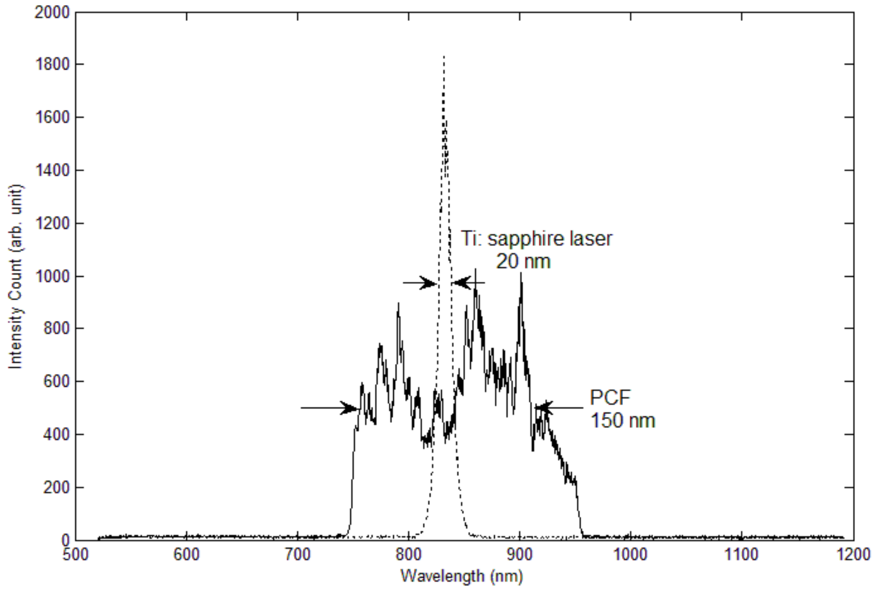

Figure 3.5 The spectrum bandwidth comparison of the laser source before and after entering the PCF

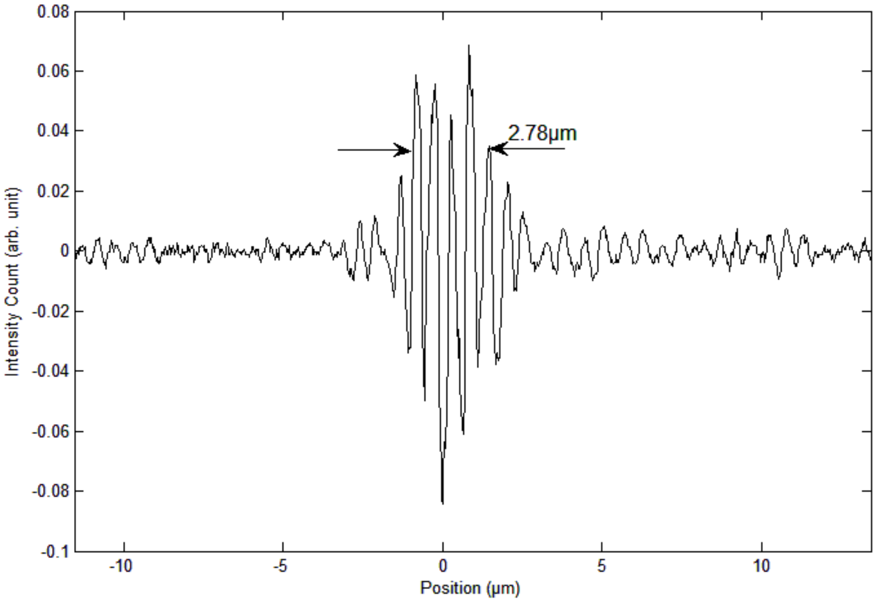

Figure 3.6 Axial resolution measured by scanning the reference arm in the axial direction and recorded with an oscilloscope

light source spectrum shape variance, but the axial resolution remained at a similar value.

Bessel illumination was characterized in comparison with Gaussian illumination. We placed a piece of paper along the propagation direction of the light and caught a sectional image of the intensity distribution of both illuminations. The edge of the distribution pattern was more clearly defined over the entire range of propagation when captured by camera in Bessel illumination than in Gaussian illumination (Figure 3.7), indicating the former had better positional stability than the latter.

To characterize the DOF of both illuminations, a Zeiss axicon camera was used to record intensity along the axial direction after the light exiting objectives. Same-source intensity and intensity degradation (neutral density filters ND1=1dB and ND2=2dB) were applied for both illuminations, and the results were shown in Figure 3.8.

Since the intensity count was saturated (Figure 3.8), we applied higher intensity degradation filters to measure the DOF of the Gaussian illumination. The result, 25.4 μm, was compared with the theoretical value of 13.7 μm acquired from Eq 3-4. Since the incident Gaussian beam failed to fulfill the rear aperture of the objective, leading to decreased NA, the measured DOF was significantly larger than the mathematical value. In contrast, a beam with the same diameter, but Bessel distribution incident to the objective was capable of 2.03 mm focusing range. This value was desirable for the study reported here because there was approximately 2 mm distance between the location of the

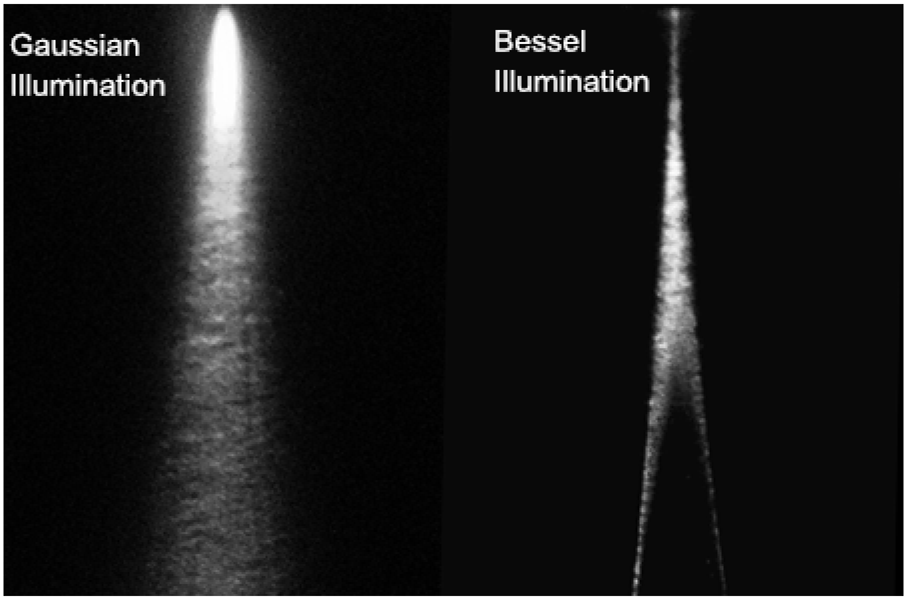

Figure 3.7 Comparison of distribution pattern and positional stability of Bessel illumination and Gaussian illumination

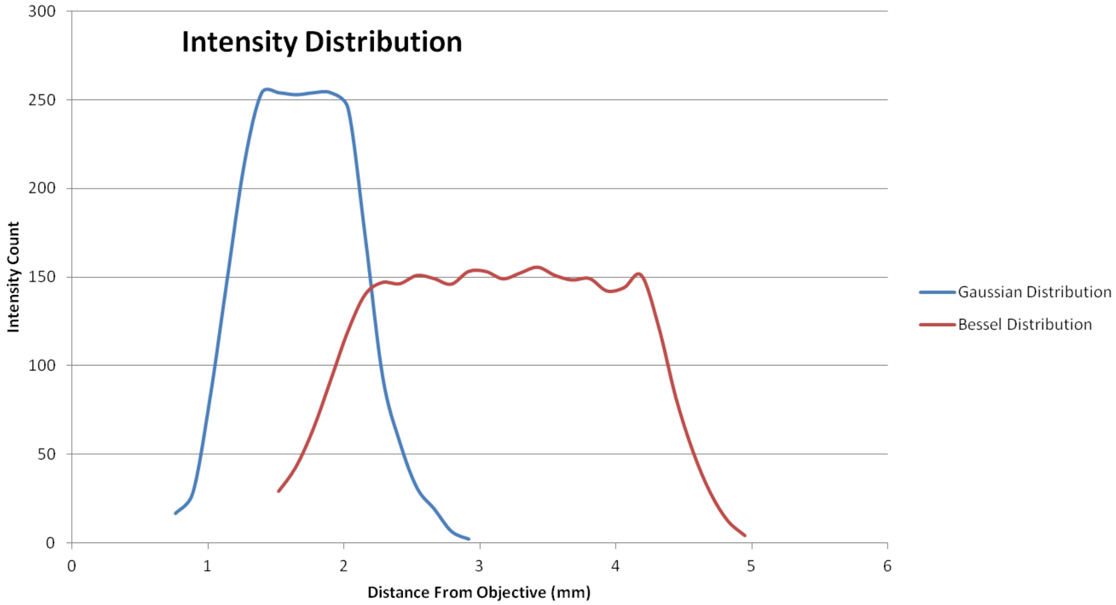

Figure 3.8 Intensity distribution of Gaussian and Bessel illumination measured with CCD camera scanning axial direction and analyzed in ImageJ.

microfluidic channel and the surface of the channels in the axial direction. The documented working distance of the objective using Bessel illumination was 3.5 mm, while the measured distance was 3.17 mm, which is caused by both the diameter of incident beam failing to fill the rear aperture of the objective and imperfection in optics alignment.

To exam the extended DOF we compared the OCM B-scan images of cover glass using Bessel and Gaussian illumination (Figure 3.9). With Bessel illumination the top and bottom boundaries of NO.1 and NO.1.5 cover glasses were clearly demonstrated while only the top boundary was shown on image with Gaussian illumination (the vague lines were reflections from other surfaces). The Bessel illumination B-scan images take over 100 pixels and 118 pixels for the thickness of NO.1 and NO. 1.5 cover glasses respectively, resulting in a proportion of 1.18. The thicknesses of the two cover glasses were later calibrated using conventional microscopy and measured thicknesses of 166 μm and 192μm for NO.1 and NO. 1.5 cover glasses respectively were obtained. This measured thickness proportion agreed with the proportion illustrated on B-scan image, indicating a good linear relation of the input and output of our system

To determine the full range of DOF we chose a slide (1mm thickness) as the sample. Since the depth range of OCM system, which is limited by the spectral resolution set by CCD sensor size [68], was 1.49 mm, the sample thickness should be smaller than the depth range. Figure 3.10 showed B-scan image of top and bottom boundaries of slide

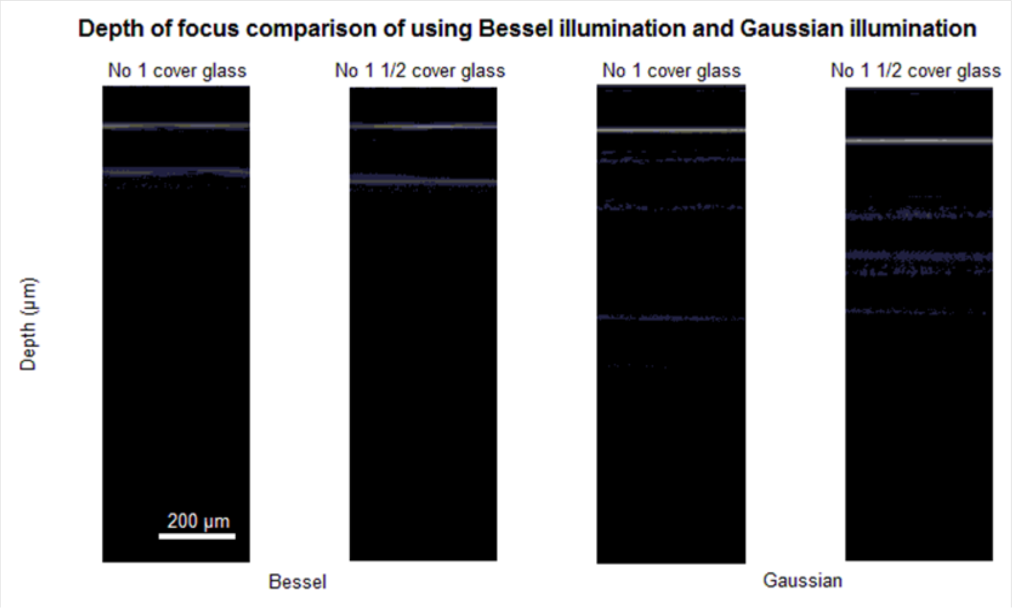

Figure 3.9 B-scan image of No.1 and No.1.5 cover glass using Bessel and Gaussian illumination. Intensity of beam in sample arm was degraded 10 dB when applying Gaussian illumination to avoid saturation.

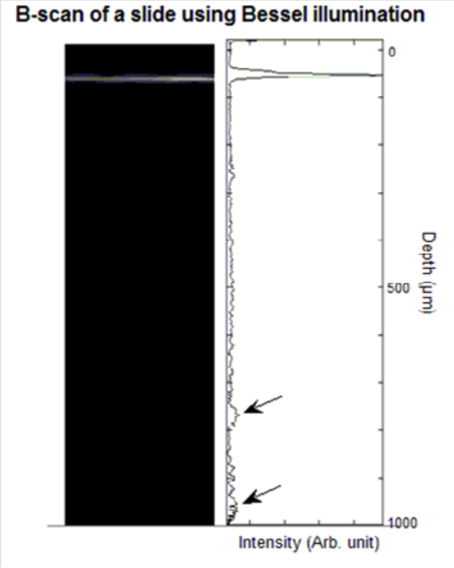

Figure 3.10 B-scan image of a slide using Bessel illuminated OCM. Arrows: two edges of the line shown on image dictating the bottom surface of the slide.

using our system. Although the bottom boundary intensity is weak, it can be illustrated by intensity plotting along axial direction. The small peaks (arrows) indicate location of bottom boundary location. The boundary line is so broadened that there are two peaks marking the beginning and end of boundary line. This phenomenon is caused by dispersion mismatch between two arms of the OCM system and will be discussed and solved in CHAPTER 4 . As a result, due to dispersion and intensity degradation of incident Bessel beam, the system was only capable of imaging 1 mm slide.

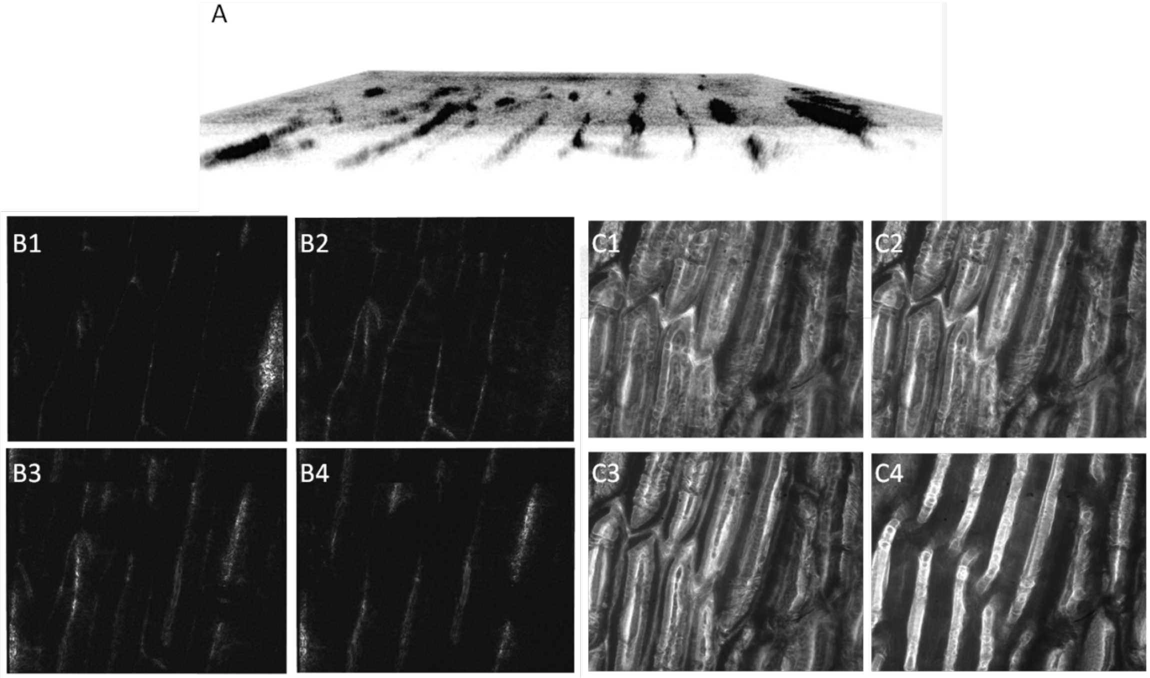

Figure 3.11 One layer of onion cells using Bessel illuminated OCM. A: 3D rendering of cells. B series: enface image in different depth of cells. Depth: B1=0 μm, B2=20μm, B3=40μm, and B4= 60μm. C series: layers at corresponding locations to B series using Gaussian illumination conventional microscope.

With the obtained Bessel illumination we applied the system in imaging one layer of onion epidermal cells. Figure 3.11 A showed the 3D reconstruction of cells with the glass surface they attached to. Unlike conventional Gaussian illuminated OCM, our system was capable of visualizing the entire depth of a cell layer by single A-scan. Figure 3.11 B series are enface images of the onion cells scanned in axial direction. And C series are the validation of these depth scans using a conventional microscope. A set of distinct border structure is observed in B4 comparing with the border on B2, indicating two cell layers were illustrated.

3.4 **Discussion**

With Bessel illumination we successfully extended the DOF 80 fold as with Gaussian illumination and practically achieved a max of 1 mm DOF by imaging a slide. The system was also applied to image biological tissue. The result showed detailed structure of one layer of epidermal onion cells over a DOF of about 80μm.

A major problem with Bessel illuminated OCM system is the small portion of energy contained in the central lobe, which is the obstacle for in vivo imaging of biological tissue in the future. The Bessel beam is power wasteful compared with Gaussian beam because it has extensive side lobe structures. This small fraction of power in central lobe leads to decreased SNR in comparison with Gaussian illumination with the very same imaging set up as shown in Figure 3.11 and Figure 3.11. The Fresnel number of our system was N_f=8.31, resulting in only about 10% of power concentrated in the central lobe [69]. While in Gaussian illumination over 70% of power was reserved in the central lobe. This is especially problematic when the biological sample is being illustrated because the lack of transparency will prevent light from penetrating. To address this problem we can replace the axicon with a spatial light modulator (SLM) to generate Bessel beam with Fresnel numbers smaller than 2 such that over 30% of power can be retained in the central lobe [69].

CHAPTER 4 MODIFICATION OF THE OCM TO ACHIEVE THE PIV IMAGING FUNCTION

4.1 **Introduction**

PIV images feature two consecutive flow field images illustrating particle position with a time interval short enough to cross-correlate the two images. Therefore if an OCM modality were to display a PIV imaging function, the system should be able to 1) illustrate particle position within the field of view, especially in the axial direction, and 2) scan sufficiently fast to cross-correlate two images in a sequence with a defined time interval between these two images. Although the claimed 3D resolution of the proposed OCM system is sufficient for illustrating a 10μm particle, the dispersion mismatch between the sample and reference arm of the interferometer in the OCM system will cause significant degradation of axial resolution, causing decreased visibility of particles deep beneath the surface of flow. Dispersion mismatch is a serious problem because 1) the system operates with a broadband spectrum, of which light of different wavelengths travels at different speeds and separated optical paths, and 2) the application of the system makes light going to the sample arm of the OCM system transmit through the sample medium while light going to the reference arm does not. Therefore, dispersion must be compensated for to achieve a PIV image of maintained resolution level.

Chromatic dispersion is the phenomenon that phase velocity and group velocity of light transmitted through media depend on frequencies of the light's components[70], e.g., red light travels faster than blue light. Because of the broad band spectrum used in the OCM system, chromatic dispersion must be corrected to avoid deterioration of axial resolution. Since group velocity is often considered at which signal conveys, only group velocity dispersion (GVD) needs to be compensated for between the two arms in an OCM system. Chromatic dispersion is defined via the Taylor expansion of wave number k[70]:

$$\begin{aligned} \mathrm{k}(\omega) = \mathrm{k}_0 + \frac{\partial \mathrm{k}}{\partial \omega}(\omega - \omega_0) + \frac{1}{2}\frac{\partial^2 \mathrm{k}}{\partial \omega^2}(\omega - \omega_0)^2 \\ + \frac{1}{6}\frac{\partial^3 \mathrm{k}}{\partial \omega^3}(\omega - \omega_0)^3 + \cdots \end{aligned} \qquad \text{Eq 4-1}$$

Where ω and ω_0 are angular frequency and center angular frequency, respectively. The constant term is the wave number at frequency ω_0. The second term is the inverse of group velocity. The third term is the GVD per unit length, which actually broadens the pulse of the incident laser and worsens the axial resolution[71]. The fourth term is third-order dispersion, which is responsible for producing asymmetric pulse distortion[71]. This equation also validated that the factors in chromatic dispersion that will affect the axial resolution, i.e., the bandwidth of the pulse in a femtosecond laser, are the third and fourth terms, which are directly linked with GVD.

Unlike traditional PIV imaging that uses two pulse exposures to take a picture of the flow field, the proposed system will scan the sectional plane along the flow direction to acquire images. Thus the time interval of two consecutive images is not determined as accurately as that in conventional PIV, especially when the Galvo scanner operating at a frequency over 250 Hz is unable to maintain the same speed during the change of scanning direction required with unidirectional scanning. The nonlinearity of the scanner position during change of direction makes it difficult to determine the speed of flowing particles. Consequently, the scanning mechanism of a Galvo scanner, together with imaging the field of view, shall be carefully determined for measurement of particle flow velocity.

4.2 **Materials and Methods**

In the OCM setup, achieving the axial resolution that meets the theoretical value requires a dispersion match in the two arms of the interferometer over the bandwidth of the light source. Two major mismatches are: 1) the mismatch caused by different optics between sample and reference arms (fixed optical paths mismatch); 2) the mismatch caused by sample penetration (variable sample penetration mismatch). Given the presence of these two mismatches, we will adjust the optical path length of the reference arm to balance the GVD.

Fixed optical paths dispersion mismatch compensation

When the light going through a sample and the reference arm travel in different optical paths, for instance, and light is transmitting through fewer lenses in the reference arm than in the sample arm, then a dispersion mismatch occurs between the two arms because the light in the reference arm experiences fewer dispersive procedures. The most common solution to fixed optical paths dispersion mismatch is to apply a dispersive medium (such as glass) plus a pair of prisms in the arm that experiences fewer dispersive procedures.

The mechanism underlying this method is as follows: When the incoming light containing a broadband frequency spectrum enters the first prism, chromatic dispersion happens, in which red light travels faster and is transmitted through the prism via a different path than blue light as shown in Figure 4.1. This chromatic dispersion is positive dispersion: The dispersed light presents a spectrum distribution before entering the second prism, where red light travels longer optical paths in media than blue light and they propagate parallel to each other upon exiting. Since red light no longer travels faster than blue light due to an elongated optical path, the dispersion that occurs in the second prism is called negative dispersion. The combination of positive and negative dispersion enables a continuous adjustment of dispersion value by means of shifting the relative position of the two prisms. After the reflection mirror placed perpendicular to the parallel propagating spectrum after the second prism, the light travels back following the incoming paths and eventually, the emitted light has every frequency component traveling the same optical path. This dispersion compensation prism pair is usually placed at the reference arm, whose end is a reflecting mirror that acts as the mirror after the second prism. A fixed shape dispersive medium is added before the prism pair when the mismatch between the sample and reference arm is bigger than the compensating range of the prism pair.

In our modality, the sample and reference arm dispersive optics were designed exactly the same to eliminate dispersion mismatch. A piece of NO.1.5 cover glass (Fisher Scientific #1) plus a pair of prisms were placed at the entrance of the reference arm to finely compensate for the dispersion produced by the cover glass on the microfluidic channel (latter described in section 5.2). Position of prism pair was continuously

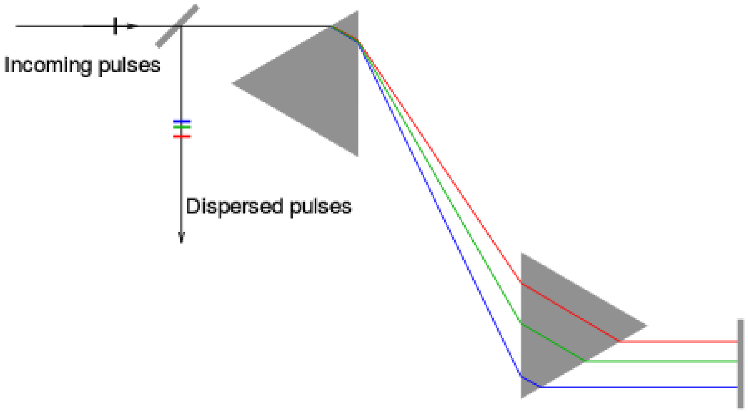

Figure 4.1 Diagram of a dispersion compensation prism pair working mechanism [72]. Image downloaded from https://en.wikipedia.org/wiki/File:Prism-compressor.svg.

adjusted in the plane perpendicular to the beam transmitting direction so that axial resolution reached its optimal value.

Variable sample penetration caused dispersion mismatch compensation

To compensate for GVD caused by individual samples of different axial imaging ranges, we post-processed the Fourier domain image using Matlab[71]. This software-based automatic dispersion compensation method was demonstrated by Fujimoto's group in retina imaging. Retina embraces similar axial range and refractive index with ours. The basic idea of this dispersion compensation processing is illustrated in the following figure extracted from the original paper: 1) Subtract the background information by deducting the signal acquired only from the reflection reference arm from the interference fringe; 2) Rescale the signal for its conversion from special domain to frequency domain and resample it with linear spacing; 3) Perform the Hilbert transform to generate the imaginary part of the complex signal from the original signal acquired from the CCD. The complex signal $\hat{S}(\omega)$ =$|S(\omega)|\exp(i\phi(\omega))$, composed of the real part obtained by CCD and the imaginary part obtained by the Hilbert transform, will be used in the following analytic processing; 4) Add the phase correction $\Phi = -a_2(\omega - \omega_0)^2 - a_3(\omega - \omega_0)^3$ to the generated signal $\hat{S}(\omega)$ to balance GVD and third-order dispersion, where a_2 and a_3 are the coefficients for these two corrections, respectively; 5) Perform a Fourier transform with the modified signal to obtain the axial depth scan; 6) Calculate the value of function

$\mathrm{M}(\mathrm{a}_2, \mathrm{a}_3)$, which defines the sharpness of the image, before adjusting the values of a_2 and a_3 until M reaches a maximum.

In our approach, $\mathrm{M}(\mathrm{a}_2, \mathrm{a}_3)$ will be defined as one divided by the total number of points in the axial scan intensity, which essentially measures the concentration of energy in the image. By iteratively varying the value of a_2 and a_3, dispersion may be automatically compensated for when $\mathrm{M}(\mathrm{a}_2, \mathrm{a}_3)$ is optimized. The cross-sectional image of ECH in HH18 that we previously obtained was used to test the feasibility of this program because it presented more layers and features than the microfluidic channel we were planning to image.

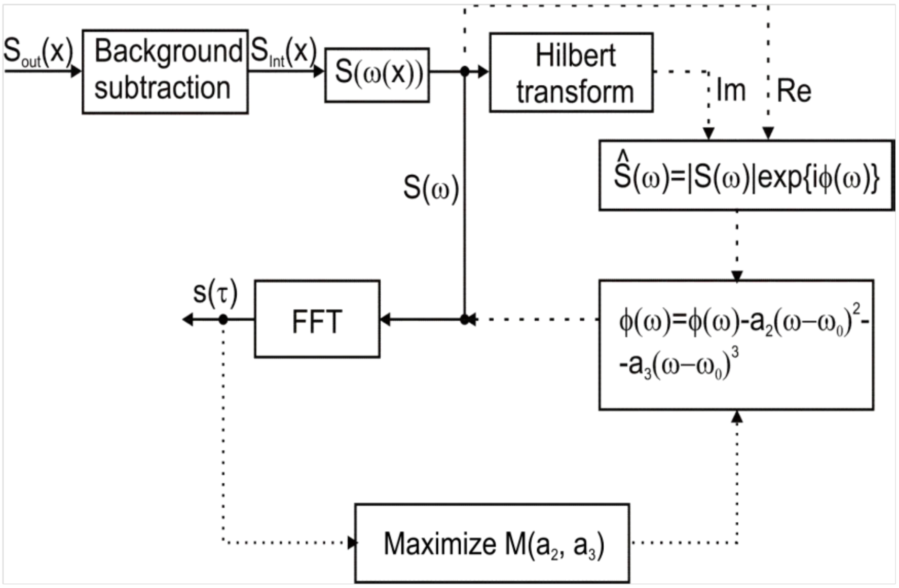

Figure 4.2 Flow chart of procedures to perform dispersion compensation.Image adapted from [71] with permission from Optical Society of America, copyright 2004.

Subframe method to increase imaging speed

The imaging speed (B-scan speed) is primarily limited by the camera triggering rate. The camera we applied was E2V AViiVA EM4 line scan CCD that allowed a maximum line rate of 70 kHz. To obtain stable exposure time and high SNR, we set the line rate at 50 kHz, corresponding to a 50 Hz frame rate with default 1000 lines/frame setting. This frame rate is insufficient to measure flow at the embryonic heart looping stages, which is about 10-20 mm/s.

To solve this problem, we divided the default frame (1000 lines) into five pieces, with each subframe consisting of 200 lines, yielding a pixel resolution of 0.5 μm in the direction of the flow (lateral direction). To achieve the subframe, the Galvo scanner in the X direction was set at five times the frequency of the frame rate (250 Hz), resulting in a measurable velocity range of 2.5-22.5 mm/s.

Calibration of scanner and linear scanning area selection

The 2D scanners used in our system are large beam diameter Galvo scanners (Thorlabs GVS012), which are capable of 1 kHz when operating at a small angle ($\pm 0.2°$). However, when the scanners work at this angular range, the field of view of the image corresponds to 60μm, which is insufficient for PIV image functionality (designed to be over 500μm). To meet the requirements of scanning speed in a certain field of view (FOV), both the amplitude and frequency of the input signal wave must be carefully selected.

When set to 250 Hz and an input angle of ±0.56°, the Galvo X scanners (responsible for B-scan) maintain linear scanning with a saw tooth wave form operating at an output angle of ±0.5°, corresponding to a field of view of 153.59 μm. In this range, a linear scan is maintained only in 74.6% of one period as shown in Figure 4.3 because of 1) fall off time of the saw tooth wave and 2) an aberration of the output wave when the scanning direction is changed. During each acquisition of a B-scan, the feedback of the scanner position will be stored and used for subtraction from the original field of view to ensure linear scanning over the entire range of the imaged area.

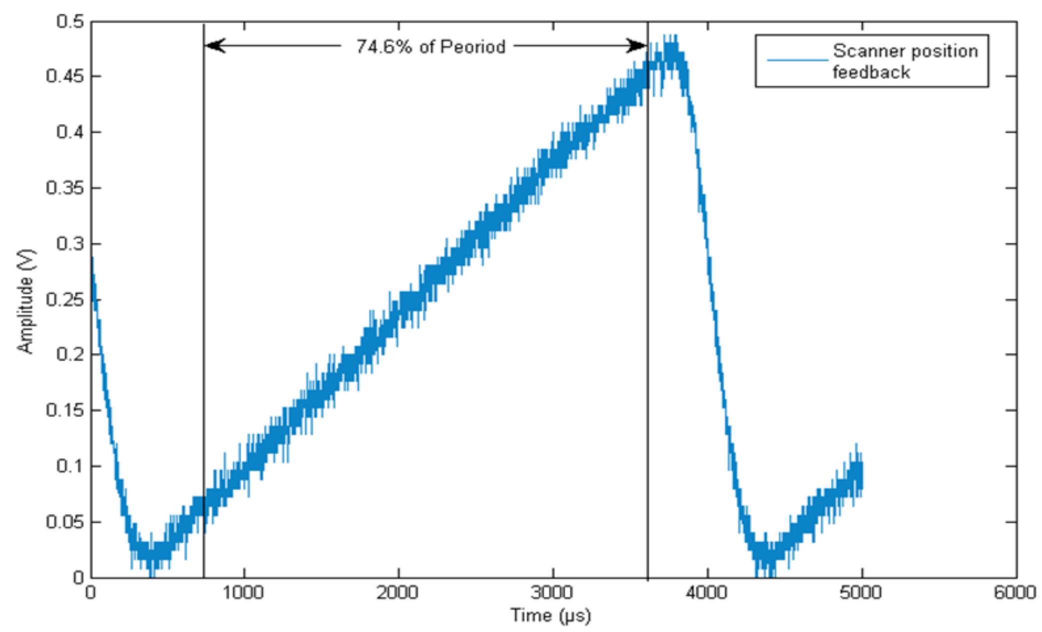

Figure 4.3 Measured feedback signal of x scanner when operating at ±0.56°, yielding a linear scanning of 115 μm.

4.3 **Results**

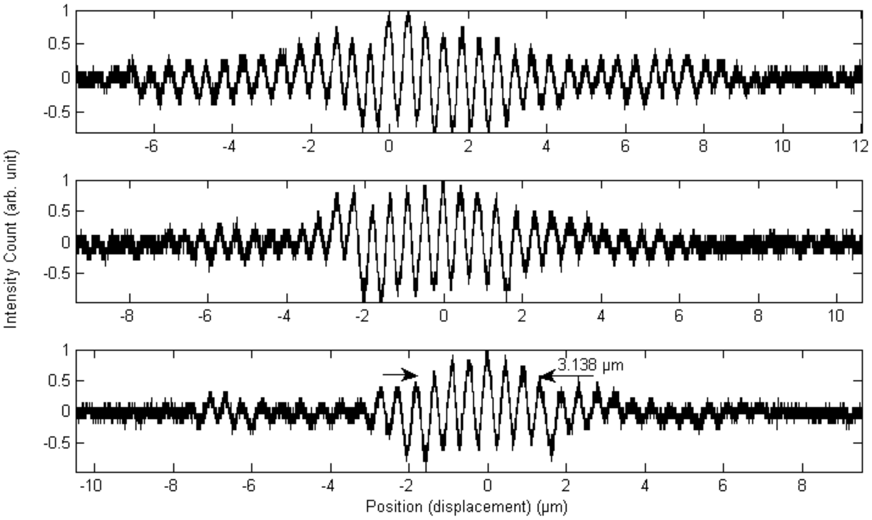

Figure 4.4 Axial resolution measurement by gradually changing the thickness of dispersion compensation prism pair. The reference arm is intentionally aligned with the Gaussian illumination to create a dispersion mismatch.

To demonstrate the dispersion mismatch taking effect on axial resolution in the OCM system, we intentionally replaced the Bessel illumination with Gaussian illumination in the reference arm. The sample arm automatically experienced more positive dispersion than the reference arm because more optical elements, such as the axicon, were needed to create Bessel illumination. Then, we placed a piece of bulky BK7 glass and a pair of optical wedges at the entrance of the reference arm to coarsely and finely compensate for the dispersion caused by the axicon and other optical elements in sample arm respectively. The advantage of an optical wedge over a prism pair is that the former changes the optical axis of the original alignment more slightly than the latter so that by shifting the position of optical wedge, one can finely adjust the dispersion without realignment of the system. By gradually shifting the optical wedge pair together, we obtained the axial resolution measurements at the zero order diffraction position shown in Figure 4.4. It is obvious that with continuous dispersion mismatch correction, the axial resolution of a Gaussian illuminated reference arm OCM system was optimized at the value of 3.14 μm, in comparison with 2.78 μm when both arms applied Bessel illumination. Further, the SNR dropped dramatically because of the dispersion compensation optics in comparison with Figure 3.6. As a result, a perfect match of optics ensured the axial resolution resemble the theoretical value of the system.

With a dispersion compensation-processing program, we obtained Figure 4.5 and Figure 4.6. In Figure 4.5 the cross-sectional image of HH18 ECH OFT is displayed. All of the layers sitting across the entire depth of focus have better-defined boundaries and become thinner after the program processing, indicating a better axial resolution. The DOF was several hundred micrometers, which was greater than our target DOF of 100 μm, indicating the feasibility of using this program in post-processing PIV images. Since PIV imaging is performed with a B-scan at the same location, only one group of dispersion compensation parameter a_2 and a_3 are required, which is sufficiently fast before calculating velocity vectors.

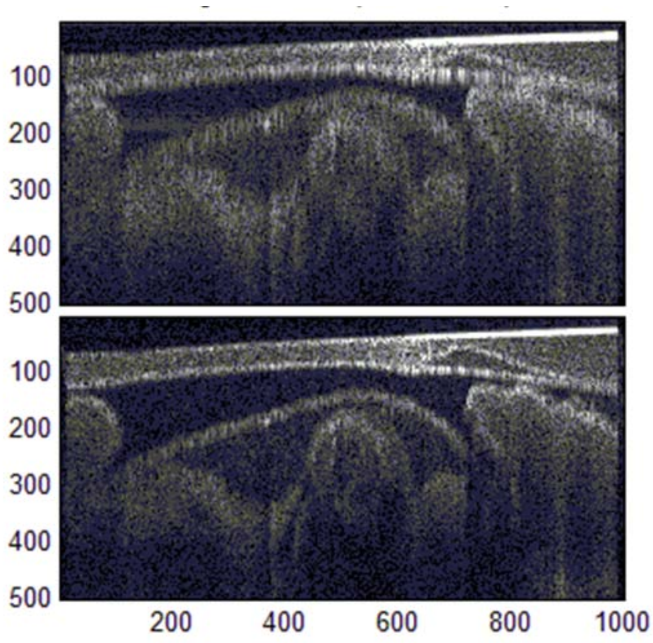

Figure 4.5 Comparison of dispersion compensation effect using software. The images are B-scan of HH18 ECH OFT with previously constructed OCT system.

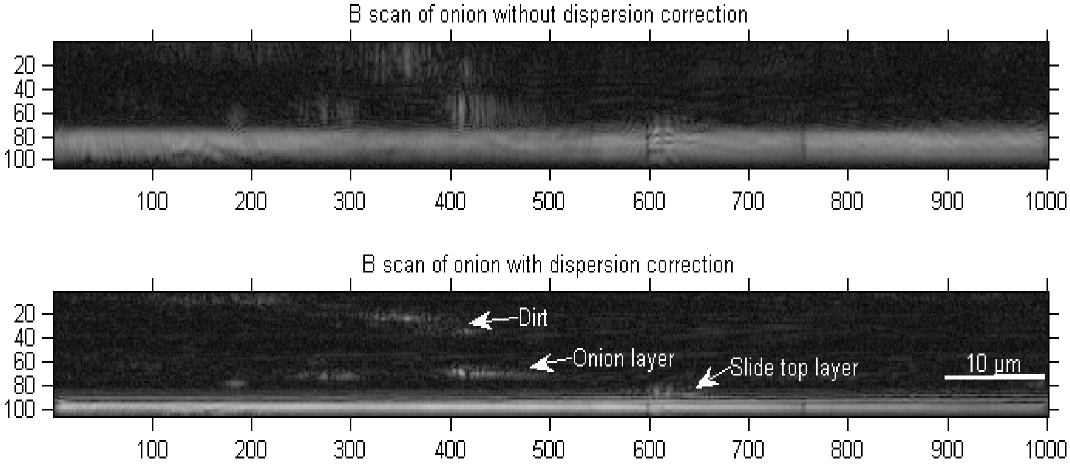

Figure 4.6 Comparison of one B scan of an onion before and after dispersion compensation.

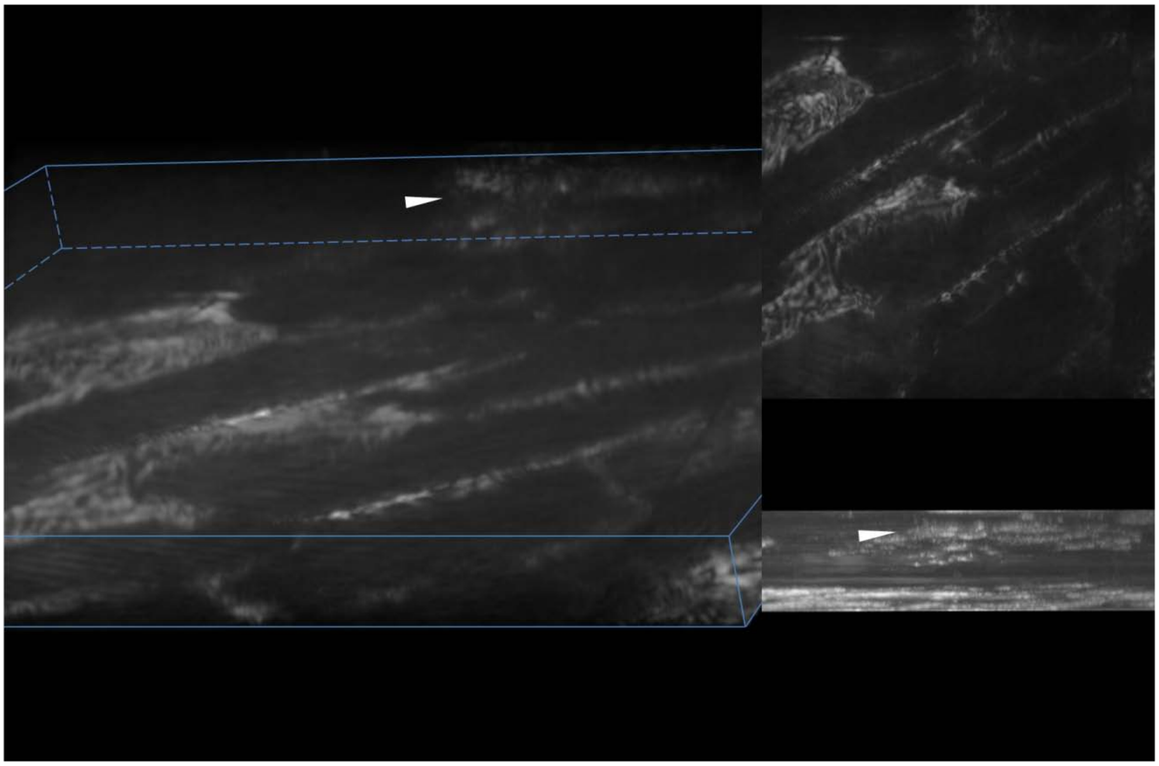

Figure 4.7 3D reconstruction of a single layer of onion cells sitting on a slide with a NO. 1.5 cover slide. Arrow: Dirt above onion cells.

Figure 4.6 demonstrates the axial resolution optimization ability of the program to discern small objects in a very thin layer (less than 100 μm) placed under a NO.1.5 cover glass. The dispersion produced by a cover glass resembled the practical situation when imaging a microfluidic channel since the channel would be sealed to a same thickness cover glass. With dispersion produced by the cover glass, the dirt and onion cells signals deteriorated to such a degree that it was difficult to differentiate each other and define their axial location (Figure 4.6 top). After applying dispersion correction program, the dirt and onion cells were separated where dirt floating at the top and the onion layer was adjacent to the slide that held the sample (Figure 4.6 bottom). The dehydrated onion created a thin layer of cells (~10 μm), which increased the difficulty for the program to differentiate it from glass. In Figure 4.7, the onion layer was verified by 3D reconstruction and displayed from the top view (C-scan). The cells showing high intensity were dead because of dehydration, and the signal came from the scattering of their cell walls. From the volume display, the onion cells and dirt were clearly defined with high resolution in both lateral and axial directions. Thus, this program was able to discern small particles in the axial direction.

The subframe image was acquired when the X scanner was scanning at the speed of 250 Hz, during which 200 camera triggers were performed to compose one subframe B-scan. This resulted in a 4μm per pixel resolution in the lateral direction, which was sufficient to visualize our tracer particle that will be introduced in section 5.2 . The velocity data can be extracted from the linear scan area based on Figure 4.3 of each subframe B-scan as shown on the opaque area of Figure 4.8.

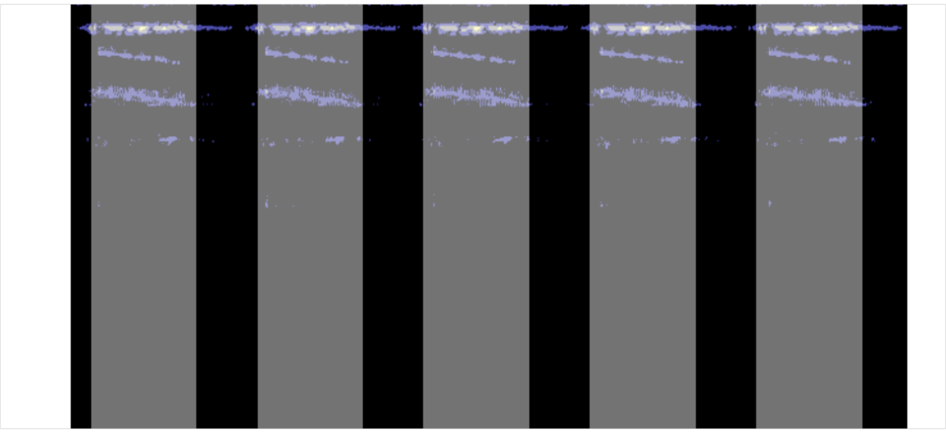

Figure 4.8 B-scan image of microfluidic channel using subframe method. Opaque areas are the linear scan area determined by the position feedback signal of X scanner.

4.4 **Discussion**

With corrected dispersion mismatch between the sample and reference arm in our OCM system we were able to provide cellular level resolution over DOF when imaging dispersive sample, such as ECH and onion cells sealed by cover glass. This modification of our system made it feasible to visualize small objects over DOF on B-scan, which was required for PIV imaging. We also successfully elevated the imaging speed 5 fold by using subframe method, resulting in a measurable flow velocity range of 2.5-22.5 mm/s.

However, when the broad band light transmitted through the axicon twice not only the dispersion mismatch but also dispersion caused by individual arm deteriorated the image resolution, sensitivity, and DOF. This was because the dispersed light failed to focus on the camera plan. Therefore, to further adapt the system for imaging highly diffractive media, such as biological samples, the light scattered from the sample should not transmit through the axicon twice in the future. To meet this target, we will either replace the axicon with the SLM aforementioned in section 3.4 or redesign the system to move the axicon lens prior to beam splitter. Compared with the first approach, the latter will be difficult because the beam ring borders and optical axis of the ring will not be parallel aligned without entering axicon for a second time. So, replacing the axicon with the SLM is the optimal choice for both power conservation and resolution maintenance over DOF.

CHAPTER 5 APPLY THE DEVELOPED SYSTEM TO A MICROFLUIDIC SYSTEM

5.1 **Introduction**

To demonstrate the feasibility of OCM-based PIV system in measuring particle velocity and illustrating the velocity map, we will create a static flow field with particles travelling through this field at given velocities. To address this design, a microfluidic system (MFC) consisting of a straight channel with rectangular cross-sections made of polydimethylsiloxane (PDMS); a syringe pump driving fluid with microbeads into this channel will be applied as the model. Constructing a cube-shaped channel with PDMS is an ideal option for demonstrating the capability of our system to illustrate fluid flow because 1) the dimensions of the channel can be conveniently determined to validate measurements acquired from PIV images; 2) the PDMS material causes negligible scattering for velocity measurements; 3) the fabrication protocol for a PDMS based microchannel is well established to eliminate structural flaws that might cause velocity field abnormalities.

After acquisition of a PIV image, particles presenting on the same sectional image do not represent their position at the same time because our system obtains a frame by scanning the longitudinal direction instead of a single exposure of the detecting camera. The time delays between scans are especially complicated when the scanner operates in a triangle waveform, as discussed in Specific Aim 2. Therefore, post-acquisition processing is needed to recover the particle to the position that corresponds to the time when the first scanning line of each frame was taken. The simultaneity of particles in the same sectional image can be realized via Matlab.

5.2 **Materials and Methods**

PDMS-based microfluidic system design and fabrication

Various microfluidic devices fabricated in PDMS have been reported for the purpose of biomedical engineering and biological studies. In this project, we fabricated a channel of 100μm X 100μm in the cross-sectional plane and 5 cm in the longitudinal direction for ease of mounting. One 1 mm and one 5 mm diameter through-holes were drilled at the two ends of the channel for flow inlet and outlet respectively. The process of fabricating PDMS microstructure has been described in detail in the literature[73]. Briefly, our process began with mask fabrication: A piece of plastic film was laser printed with microfeatures drawn in Solidworks. We chose plastic film over glass film because the former had sufficient resolution for 100 μm features and was less expensive than the latter. This film was later used as a photomask in UV-photolithography to create a master. As shown in the flow chart image reproduced and adapted from[74], a piece of wafer was plasma-cleaned and then spin-coated with SU-8 as the photoresist (MicroChem, Corp). A solution of 2ml SU-8 2075 was poured onto a 2 inch diameter wafer and spun at 2125 rpm for 30s to generate a 100 μm thick layer. The coated wafer was soft-baked at 95°C for 2 min to evaporate residual solvent and solidify the photoresist. Subsequently, the coated wafer was exposed to UV radiation (230mJ/cm^2) through the photomask for 77 seconds. The emulsion side of the photomask was placed downward in direct contact with the photoresist layer to eliminate dimensional aberration caused by diffraction of UV light. With the photomask removed, the coated wafer was hard-baked at 95°C for 3 min to complete SU-8 crosslinking. A developing reagent was used to dissolve the unexposed regions, and the resulting SU-8 structure served as the master to fabricate the PDMS channel. Liquid PDMS prepolymer (base polymer: curing agent=10:1) was poured onto the master. The PDMS mold was cured at 80°C overnight and then peeled off the master. The inlet and outlet of the fluidic channel were generated by drilling one 1mm and one 3mm diameter through-holes respectively on the PDMS mold at the end of the straight channel. Finally, the PDMS channel was sealed onto a cover glass by conformal contact to ensure a watertight condition during imaging.

Flow pumping mechanism and calibration

The pump we had access to was a syringe pump capable of up to 60 mL liquid at the velocity range from 0.008 nL/hr to 152.7 mL/hr. The pump was driven by a step motor and controlled by a keypad on the machine itself. The minimum volumetric velocity for the 10 mL syringe we applied was 167 nL/hr, which was convenient for calibration purposes. The pumping rate set at 72 μL/hr (corresponding to 2 mm/s in MFC) was

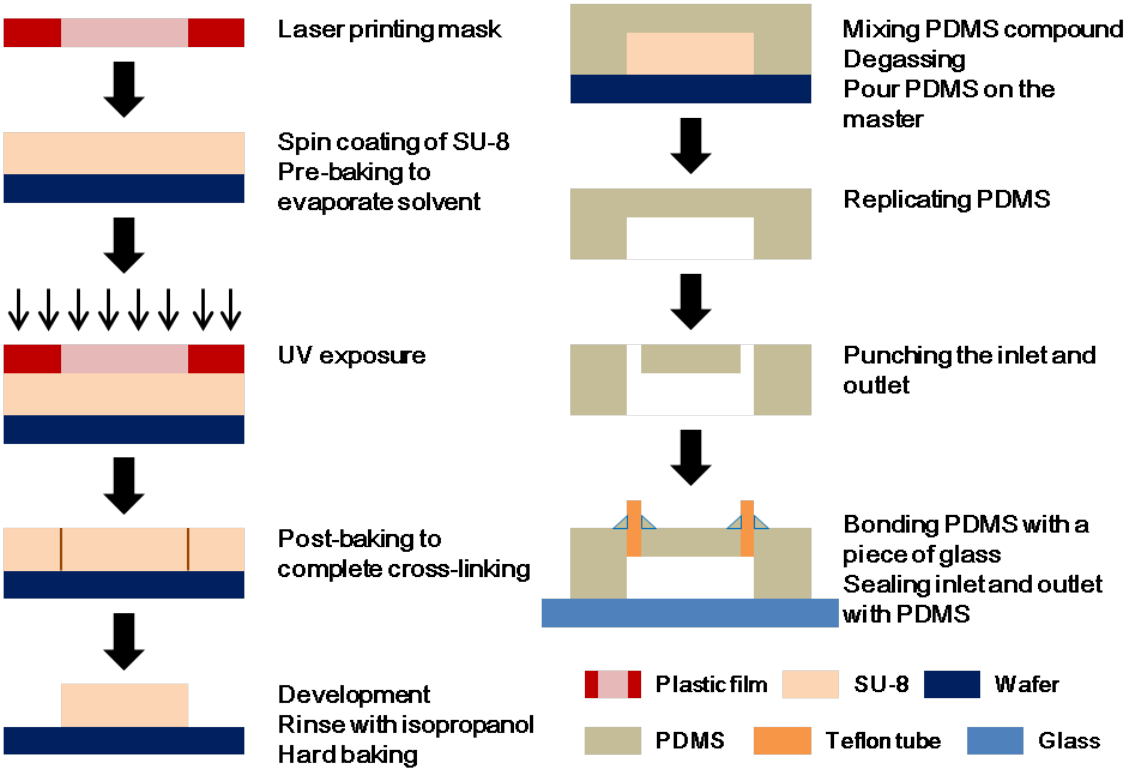

Figure 5.1 Flow chart of fabricating microfluidic channel. Image adapted from [74] with permission from John Wiley and Sons, copyright 2013.

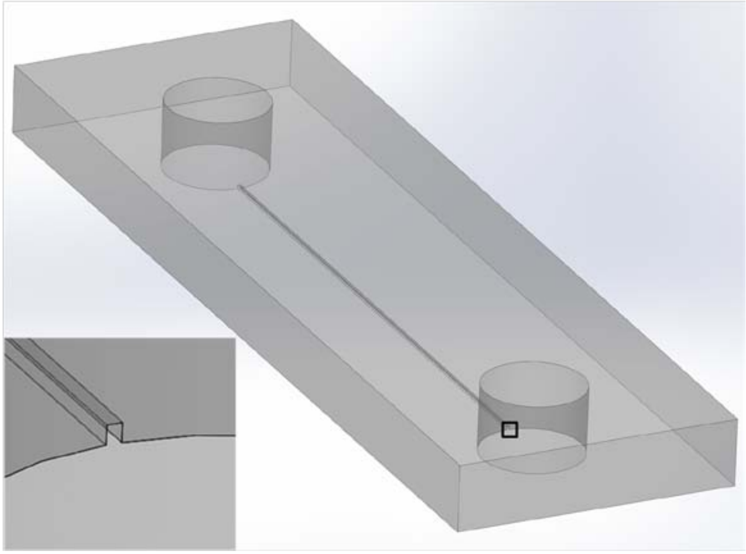

Figure 5.2 SolidWorks drawing of the microfluidic channel with designed dimensions.

calibrated by taking pictures of the syringe plumber movement using conventional microscopy and a measured value of 68.04 μL/hr was acquired. This flow rate was set to better demonstrate the feasibility of our system in flow rate measurement without using subframe method.

Tracer particle selection

The microbeads (Potter Industries, 1.05 g/cm^3 density, 10 μm diameter) that made of hollow glass and are similar in size to a red blood cell during embryogenesis stages were chosen as the tracer particle because of their similar applications in the literature [75]. If we assume the microbeads immersed flow had a typical embryonic blood vessel density of 1.025 g/cm^3, a viscosity of 0.03 P [39], gravity acceleration equals to 9.8 m/s^2, according to Eq 2-13 the settling velocity in the opposite direction of gravity is calculated as:

$$u_s=\frac{gd_p^2(\rho_p-\rho_f)}{18\mu}=\frac{9.8\times10\times(1.05\text{-}1.025)}{18\times0.03}\times\frac{10^{-9}\text{mm}}{\text{s}}=4.54\times10^{-9}\text{mm/s},$$

which is negligible compared with 2 mm/s mean flow velocity. This made the hollow glass sphere the suitable tracer particles to mimic red blood cells.

A total of 4 g of dry microbeads were mixed and then suspended in 8 mL phosphate-buffered saline (PBS) [75].

Velocity measurement using cross-correlation

The cross-correlation program we used was an ImageJ (imagej.net) plugin directly downloaded from the website. It is able to calculate the cross-correlation of a certain size of interrogation area that is selected by user in two consecutive images in one stack. And the result is given by colored arrows with a color map legend indicating displacement of interrogation area in the number of pixels. PIV sample images of tracer particles traveling in a given velocity were used to validate the feasibility of this software. To further analyze the velocity values numerically and improve the appearance of map we exported the PIV data from ImageJ to Matlab and used quiver function to draw the vector map with uniform color. The velocity map with uniform color was easier to compare velocity values in axial direction as in our case.

In our approach, we applied 16x16 pixels as interrogation area for sufficient velocity map resolution. Since OCM automatically sliced a thin cross-sectional layer, there were only a few beads captured by one single B-scan, which is difficult to calculate the velocity distribution over an entire cross-sectional area. Therefore, before calculating velocity, we stacked 15 B-scan images and use max projection in the Z direction to acquire sufficient number of tracer particles as shown in Figure 5.3. Then the stacked image was subtracted with the channel border and denoised before it cross-correlated with another stacked image.

To acquire reliable results of PIV, we selected 15 images at the time points with odd numbers (1,3,5,…) for the first stack and another 15 images at the time point of the following even numbers (2,4,6,…) for the second stack. In this way, the time interval between the two stacks was equal to the camera trigger interval (20ms as the case in Figure 5.3).

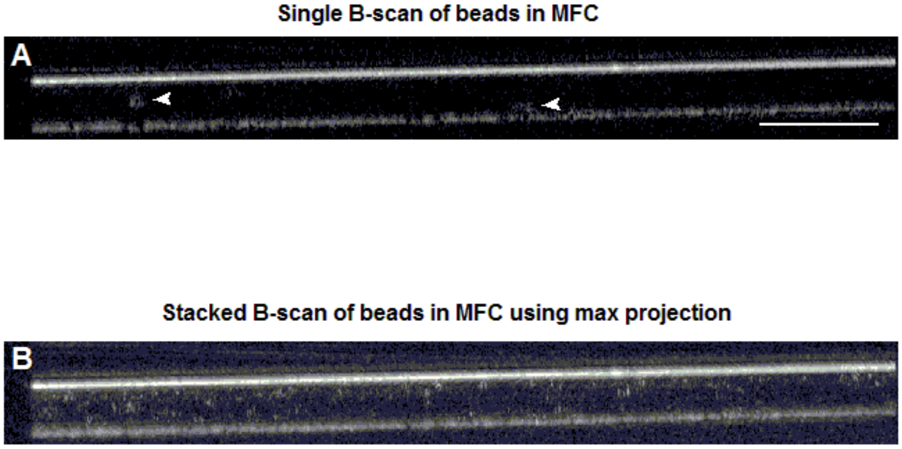

Figure 5.3 B-scans of microbeads flowing in MFC. A: before stacking only two beads as indicated with arrows appeared in B-scan. B: after 15 images stacking the channel is full of beads. Scale bar: 50 μm.

5.3 **Results**

The PDMS based MFC was successfully manufactured and plasma sealed onto a NO. 1.5 cover glass (Corning) to both ensure durability and reduce dispersion produced by the glass. During imaging, the channel was placed onto sample stage of the OCM system with the cover glass positioned on the top and PDMS on the bottom. The flow entered MFC from a tube with a pipette tip penetrating through a hole on the sample stage and connecting with the inlet. The liquid at the outlet was induced into a syringe with the same set of equipment as the inlet. The flow was pumped into the channel using a syringe pump setting at 72 μL/hr to testify the velocity measurement. The pumping velocity was validated using a conventional microscope with camera recording. The flow rate was maintained during measurement. The B-scan was selected as a plane in the center area of the MFC.

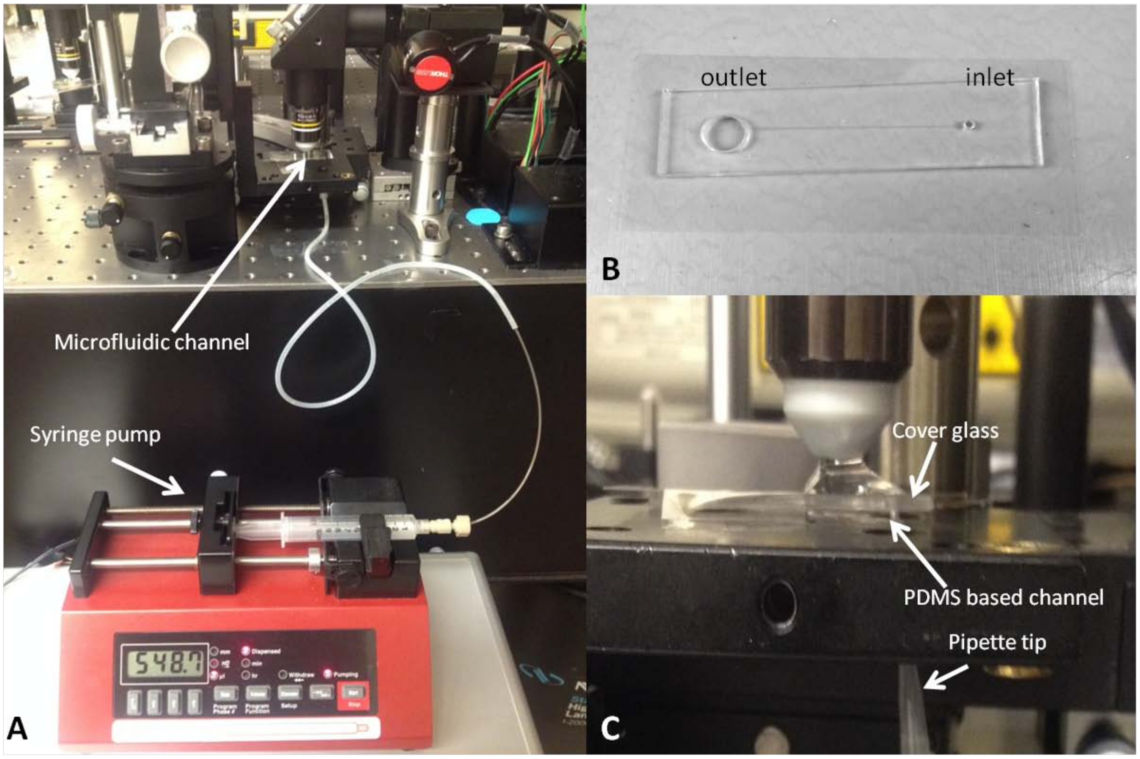

Figure 5.4 Imaging set up of measuring flow field in MFC.

To testify the ability of our system in imaging MFC of 100 μm depth at maintained resolution level, we placed the MFC in the position shown in Figure 5.4 with no fluid in it.

The top and bottom surfaces of MFC were clearly demonstrated as two parallel lines after dispersion compensation in B-scan. And 3D reconstruction of the channel provided C-scan showing details on the top and bottom surfaces. On Figure 5.5B there are wrinkles around the outside of the border on the top surface of MFC, where it attached to a cover glass. The wrinkles appeared because the cover glass was slightly bent due to fixation issues during imaging. On Figure 5.5C, the borders on the bottom surface are not perfect straight because of manufactured flaws. These details proved a good lateral resolution over DOF.

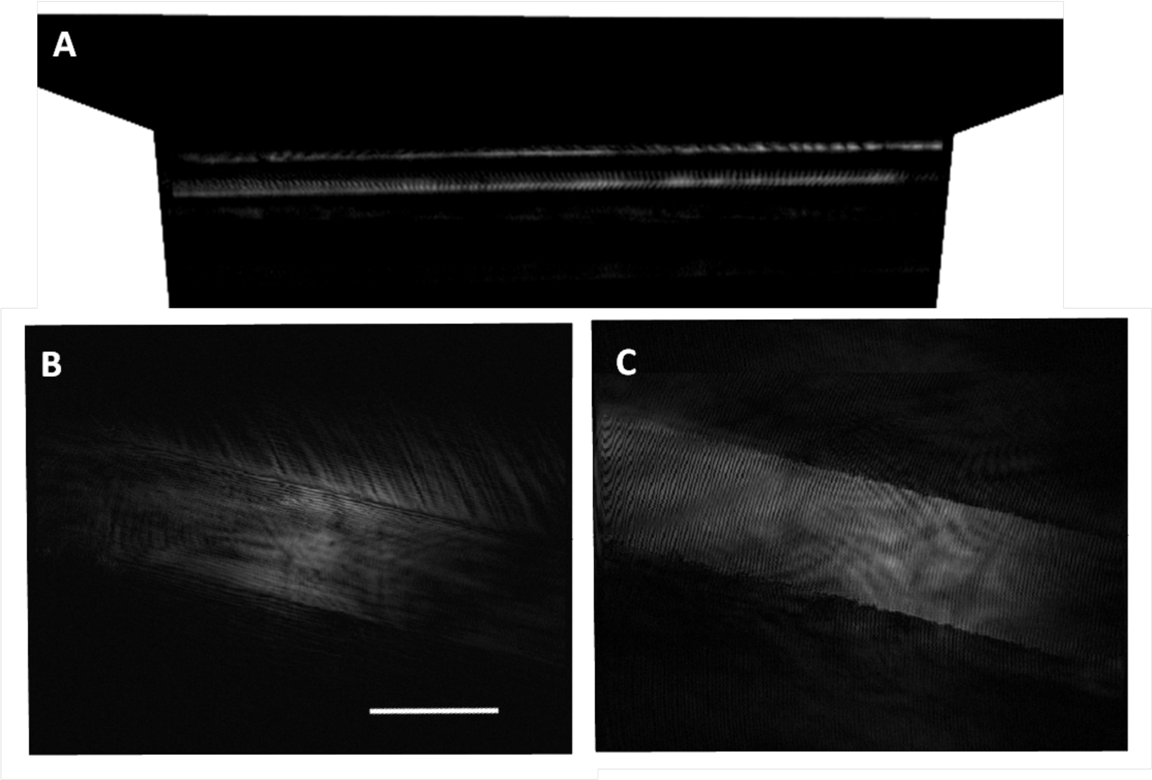

Figure 5.5 MFC images using Bessel illuminated OCM. A: B-scan of the channel. B: top surface of channel. C: bottom surface of channel. Scale bar: 100 μm.

The MFC was oriented to be parallel with the B-scan direction to acquire a FOV of 800 μm in longitudinal direction. This orientation of B-scan made it easy to capture single bead flowing path. As a result, the beads were traceable over entire FOV using our imaging modality as shown in Figure 5.6. This result validated that the particle was traveling within the plane of imaging, making it feasible to calculate velocity.

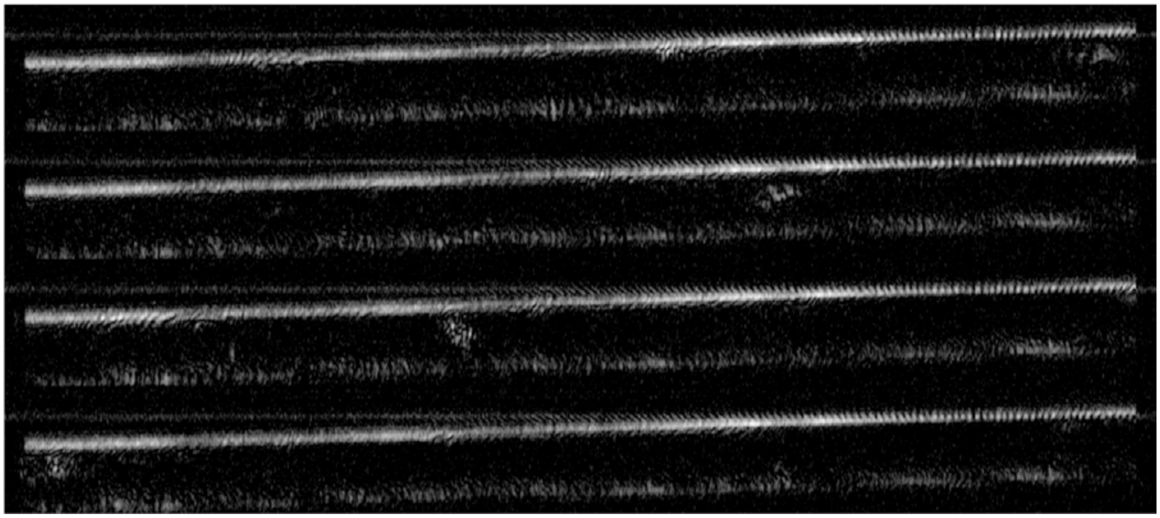

Figure 5.6 A group of aggregated beads flowing in channel.

The motion of each bead can be examined using our set up. From a series of consecutive B-scans (Figure 5.7) we observed three beads at different depths started at a similar longitudinal position. The closer to the channel center, the faster the bead travelled. This was in accordance with the laminar flow profile. The fast imaging speed and high resolution of the imaging system made it feasible to observe the motion track and calculate the velocity profile of each individual bead conveniently. The bead indicated with arrow shown in Figure 5.7 that was closest to channel center in this B-scan series was measured flowing at the rate of 3.2 mm/s.

The PIV result was calculated based on two B-scan pairs, each stacked with 15 images and interrogation area of 16x16 pixels as mentioned in section 5.2 , resulting in 8 velocity vectors along each cross-sectional line within range of MFC (128 pixels). Each B-scan was synchronized with the X scanner's position-feedback signal (saw tooth wave in Figure 5.8), and only the linear scan area of each B-scan was recorded. We took only the particles in the linear scan area that was in between the white lines in Figure 5.8 for

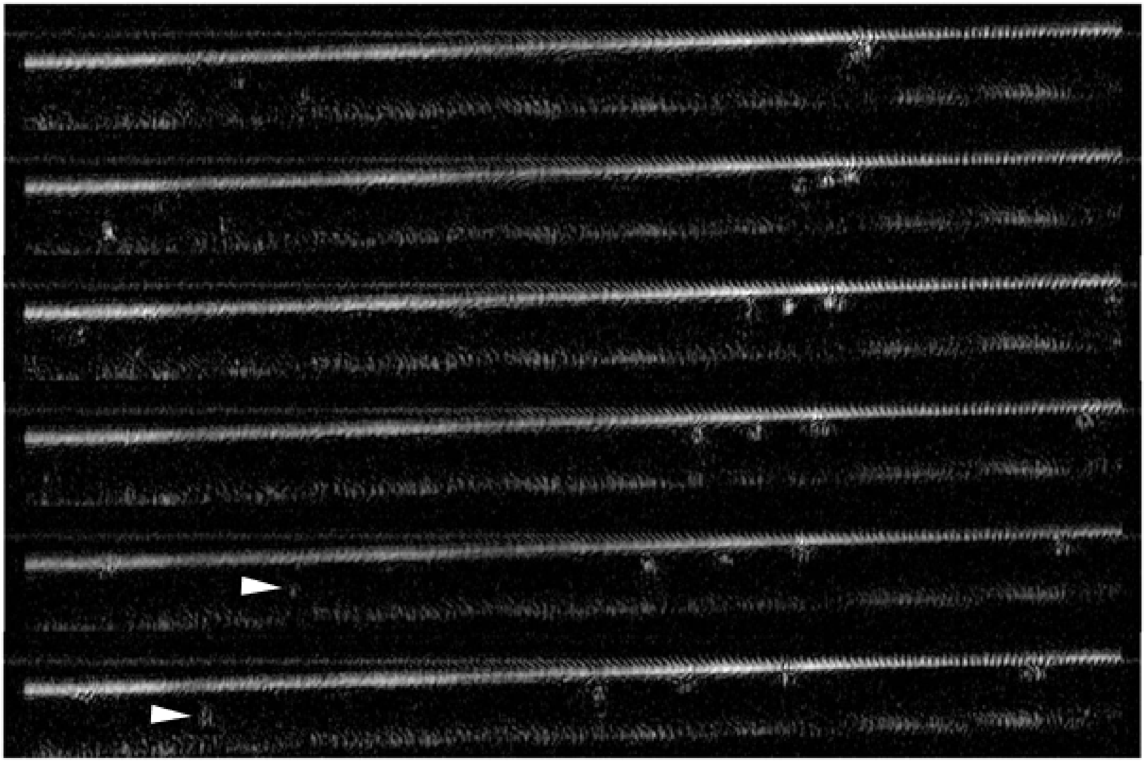

Figure 5.7 Consecutive B-scan of beads flowing in different speed. Arrow: bead close to channel center.

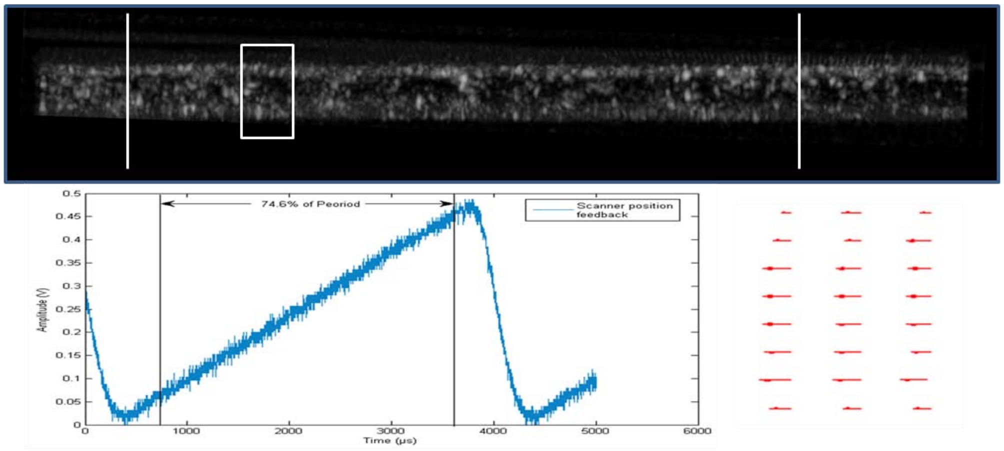

Figure 5.8 PIV result. Top: stacked 15 B-scan with linear scan area as shown in between lines, and an area of interest indicated by a rectangle; bottom left: position feedback of X scanner; bottom right: flow field velocity map of the zoomed-in area of interest.

PIV calculations. The vector map demonstrates the velocity distribution in the white rectangle area.

According to the flow rate calibrated based on the syringe-plunger movement (68.1 µL/hr), we performed a simulation of the flow in MFC using Comsol. Since it is a steady laminar flow through a channel with constant cross-section, the simulated flow profile is identical on each cross-sectional region, as shown in Figure 5.9, on the top. The lateral location of the B-scan was determined based on the C-scan and is indicated by the dotted line on the top figure. The velocity profile obtained by the B-scan for this location is illustrated as a bar graph in Figure 5.9, on the bottom. We calculate the velocity profiles at 10 selected locations evenly distributed along the B-scan direction, and the red bars in

Figure 5.9 represent a typical profile. The dotted line overlapped with the red bars was the simulated velocity distribution, which shows a max simulated velocity of 3.69 mm/s. The max velocity calculated using the PIV software (ImageJ PIV plugin and Matlab) indicated by the red bar was 3.20 mm/s, which was in accordance with the value calculated based on an individual bead displacement (Figure 5.7). The measured integration of velocity value over axial range of 100μm, indicating the flux in the longitudinal cross-section was 0.238 ± 0.0268 mm^2/s, which agreed statistically ($P = 0.05$) with the simulated value of 0.254 mm^2/s with a relative error of 6.30%.

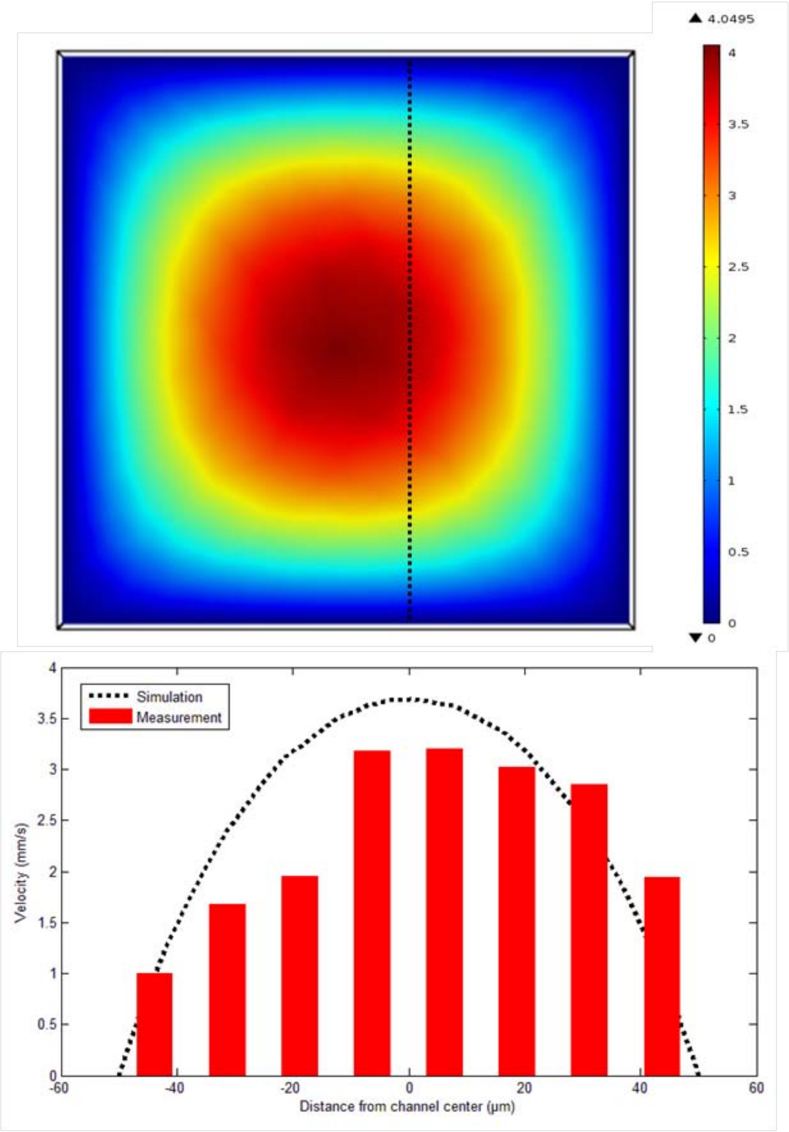

Figure 5.9 Velocity profiles based on simulation and measurements. Top: Comsol simulation result of flow velocity map in MFC; Bottom: simulated (dot line) and measured (bars) velocity distribution of the longitudinal cross-section that B-scan took.

5.4 **Discussion**

With the OCM based PIV system we were able to image the MFC structure and flow field simultaneously. The velocity measurements based on individual particle displacement and interrogation spot cross-correlation (with the dimension of the interrogation window (12.8µm by 12.8µm) being set at the scale of the particle size (10µm) agreed with each other. The measured results were validated with the simulated flux on a longitudinal cross-section with statistically acceptable error. This method presented the advantages of using shared illumination and imaging optics in contrast to conventional PIV, greater and adjustable FOV compared with µPIV, and more accurate measurement of velocity based on tracer particle movement in comparison with Doppler OCT.

There are several factors contributed to the inaccuracy of measured velocity, and the OCM-based PIV needs further modifications accordingly.

Since the flow was present in a channel with square shaped cross section, the simulated velocity distribution was not a perfect parabola, and the max velocity was bigger than twice the calibrated average velocity. The measured max velocity was smaller than the simulated max velocity of 3.69 mm/s as indicated by the dotted line in Figure 5.9. This was partially due to the lateral migration of beads as a result of bead rotation and gravity driven particle sedimentation. Near both borders the measured particle velocities were much larger than 0 mm/s. This was because when the 15 images were stacked the border information was subtracted for later noise deduction processing. The particles resided on the border were also subtracted from the stack, causing loss of stationary particles. Therefore only moving particles were calculated. At the lower side of the flow channel, the particle presented greater velocity than that at the upper side. This is mainly because the density of the class particle was larger that of the flowing media (PBS), gravity drove the sedimentation of the particles, which caused particles from high-speed layer of the laminar flow (e.g., center layer) laterally migrated to the low-speed layer (e.g., bottom layer) , making the velocity profile slightly shift toward the bottom border. In the future we will apply smaller tracer particles with a matched density when the resolution of system is elevated after modification of system as mentioned in section 3.4 .

To better simulate blood flow we will replace the syringe pump with a peristaltic pump (Langer Instruments BT100-2J) in the future since the flow during early embryonic heart developmental stages is considered peristaltic flow as noted in section 2.2 . The pump is automatically controlled by the built-in electrical and mechanical system once speed is manually set. We assumed the average flow velocity was at the range of 0-15 mm/s, yielding a max volumetric flow rate at 9 mL/min, which is within the pumping flow rate capability of precise velocity control pump head (DG-1).

In addition, the velocity vector map obtained from our current set up was different than that acquired using conventional PIV because our light sheet was formed by scanning a single beam along flow direction as opposed to a pulsed light sheet. This means the vectors on velocity map represent measurements obtained in different time point. In the future we need to adjust the map so that the PIV profile representing velocity measurements of different locations at the same time. This is especially important when peristaltic flow, instead of laminar flow is applied for imaging. After the adjustment a 3D flow measurement will be available when the system scans in the direction perpendicular to the B scan.

CHAPTER 6 CONCLUSION

We presented a Bessel illuminated OCM-based PIV system that is capable of invasively imaging biological tissue at micrometer resolution and 1 mm depth of focus at the frame rate of 250 Hz. With this imaging set up we successfully assessed velocity profile in a microfluidic system and structure details of the microfluidic channel simultaneously. Owning to high resolution and frame rate, tracer particles were illustrated clearly in B-scan, making it possible to measure flow velocity using individual particle or perform cross-correlation of two consecutive images. The OCM-based PIV modality is easier to perform in vivo imaging in comparison with conventional PIV and provides more accurate flow measurement in comparison with Doppler OCT. As a result, OCM-based PIV imaging modality makes it feasible in future application to observe in vivo the detailed biological process over long period of time, such as congenital heart remodeling in response to environmental alterations.

REFERENCE

[1] DALYs GBD, Collaborators H. Global, regional, and national disability-adjusted life-years (DALYs) for 315 diseases and injuries and healthy life expectancy (HALE), 1990-2015: a systematic analysis for the Global Burden of Disease Study 2015. Lancet. 2016;388:1603-58.

[2] Mortality GBD, Causes of Death C. Global, regional, and national life expectancy, all-cause mortality, and cause-specific mortality for 249 causes of death, 1980-2015: a systematic analysis for the Global Burden of Disease Study 2015. Lancet. 2016;388:1459-544.

[3] Congenital heart defects in children fact sheet. 2004.

[4] Hamburger V, Hamilton HL. A Series of Normal Stages in the Development of the Chick-Embryo, (Reprinted from Journal of Morphology, Vol 88, 1951). Dev Dynam. 1992;195:231-&.

[5] Manner J. The Anatomy of Cardiac Looping: A Step Towards the Understanding of the Morphogenesis of Several Forms of Congenital Cardiac Malformations. Clin Anat. 2009;22:21-35.

[6] Ramsdell AF. Left-right asymmetry and congenital cardiac defects: Getting to the heart of the matter in vertebrate left-right axis determination. Dev Biol. 2005;288:1-20.

[7] Culver JC, Dickinson ME. The effects of hemodynamic force on embryonic development. Microcirculation. 2010;17:164-78.

[8] Bartman T, Hove J. Mechanics and function in heart morphogenesis. Dev Dynam. 2005;233:373-81.

[9] Reamon-Buettner SM, Spane-Borowski K, Bortak J. Bridging the gap between anatomy and molecular genetics for an improved understanding of congenital heart disease. Ann Anat. 2006;188:213-20.

[10] Hove JR, Koster RW, Forouhar AS, Acevedo-Bolton G, Fraser SE, Gharib M. Intracardiac fluid forces are an essential epigenetic factor for embryonic cardiogenesis. Nature. 2003;421:172-7.

[11] Egorova AD, Khedoe PPSJ, Goumans MJTH, Yoder BK, Nauli SM, ten Dijke P, et al. Lack of Primary Cilia Primes Shear-Induced Endothelial-to-Mesenchymal Transition. Circ Res. 2011;108:1093-U142.

[12] Schoenwolf GC. Visualizing complex 3-D changes over time in human embryology. Faseb J. 2001;15:A66-A.

[13] Kaneko K, Li X, Zhang X, Lamberti JJ, Jamieson SW, Thistlethwaite PA. Endothelial expression of bone morphogenetic protein receptor type 1a is required for atrioventricular valve formation. The Annals of thoracic surgery. 2008;85:2090-8.

[14] Egorova AD, Khedoe PP, Goumans MJ, Yoder BK, Nauli SM, ten Dijke P, et al. Lack of primary cilia primes shear-induced endothelial-to-mesenchymal transition. Circulation research. 2011;108:1093-101.

[15] Groenendijk BC, Hierck BP, Gittenberger-De Groot AC, Poelmann RE. Development-related changes in the expression of shear stress responsive genes KLF-2, ET-1, and NOS-3 in the developing cardiovascular system of chicken embryos. Developmental dynamics : an official publication of the American Association of Anatomists. 2004;230:57-68.

[16] Van der Heiden K, Groenendijk BC, Hierck BP, Hogers B, Koerten HK, Mommaas AM, et al. Monocilia on chicken embryonic endocardium in low shear stress areas. Developmental dynamics : an official publication of the American Association of Anatomists. 2006;235:19-28.

[17] Parmar KM, Larman HB, Dai G, Zhang Y, Wang ET, Moorthy SN, et al. Integration of flow-dependent endothelial phenotypes by Kruppel-like factor 2. The Journal of clinical investigation. 2006;116:49-58.

[18] Dekker RJ, Boon RA, Rondaij MG, Kragt A, Volger OL, Elderkamp YW, et al. KLF2 provokes a gene expression pattern that establishes functional quiescent differentiation of the endothelium. Blood. 2006;107:4354-63.

[19] Nakajima Y, Yamagishi T, Hokari S, Nakamura H. Mechanisms involved in valvuloseptal endocardial cushion formation in early cardiogenesis: Roles of transforming growth factor (TGF)-beta and bone morphogenetic protein (BMP). Anatomical record. 2000;258:119-27.

[20] McQuinn TC, Bratoeva M, Dealmeida A, Remond M, Thompson RP, Sedmera D. High-frequency ultrasonographic imaging of avian cardiovascular development. Dev Dynam. 2007;236:3503-13.

[21] Ogawa S, Lee TM, Kay AR, Tank DW. Brain magnetic resonance imaging with contrast dependent on blood oxygenation. Proceedings of the National Academy of Sciences of the United States of America. 1990;87:9868-72.

[22] Kim JS, Min J, Recknagel AK, Riccio M, Butcher JT. Quantitative three-dimensional analysis of embryonic chick morphogenesis via microcomputed tomography. Anatomical record. 2011;294:1-10.

[23] Prevrhal S, Forsythe CH, Harnish RJ, Saeed M, Yeh BM. CT Angiographic Measurement of Vascular Blood Flow Velocity by Using Projection Data. Radiology. 2011;261:923-9.

[24] Butcher JT, Sedmera D, Guldberg RE, Markwald RR. Quantitative volumetric analysis of cardiac morphogenesis assessed through mirco-computed tomograpy. Dev Dynam. 2007;236:802-9.

[25] Cenic A, Nabavi DG, Craen RA, Gelb AW, Lee TY. Dynamic CT measurement of cerebral blood flow: A validation study. Am J Neuroradiol. 1999;20:63-73.

[26] Gobbel GT, Cann CE, Fike JR. Measurement of Regional Cerebral Blood-Flow Using Ultrafast Computed-Tomography - Theoretical Aspects. Stroke. 1991;22:768-71.

[27] Chen ZP, Milner TE, Dave D, Nelson JS. Optical Doppler tomographic imaging of fluid flow velocity in highly scattering media. Opt Lett. 1997;22:64-6.

[28] Chen ZP, Milner TE, Srinivas S, Lindmo T, Dave D, Nelson JS. Optical Doppler tomography for noninvasive imaging of in vivo blood flow. P Soc Photo-Opt Ins. 1997;2981:112-8.

[29] Davis AM, Rothenberg FG, Shepherd N, Izatt JA. In vivo spectral domain optical coherence tomography volumetric imaging and spectral Doppler velocimetry of early stage embryonic chicken heart development. J Opt Soc Am A. 2008;25:3134-43.

[30] Poelma C, Van der Heiden K, Hierck BP, Poelmann RE, Westerweel J. Measurements of the wall shear stress distribution in the outflow tract of an embryonic chicken heart. J R Soc Interface. 2010;7:91-103.

[31] Jonas S, Bhattacharya D, Khokha MK, Choma MA. Microfluidic characterization of cilia-driven fluid flow using optical coherence tomography-based particle tracking velocimetry. Biomed Opt Express. 2011;2:2022-34.

[32] Person AD, Klewer SE, Runyan RB. Cell biology of cardiac cushion development. Int Rev Cytol. 2005;243:287-+.

[33] Krug EL, Runyan RB, Markwald RR. Protein Extracts from Early Embryonic Hearts Initiate Cardiac Endothelial Cytodifferentiation. Dev Biol. 1985;112:414-26.

[34] Ffrenchconstant C, Hynes RO. Patterns of Fibronectin Gene-Expression and Splicing during Cell-Migration in Chicken Embryos. Development. 1988;104:369-82.

[35] Kirby ML, Waldo KL. Neural Crest and Cardiovascular Patterning. Circ Res. 1995;77:211-5.

[36] Christoffels VM, Habets PEMH, Franco D, Campione M, de Jong F, Lamers WH, et al. Chamber formation and morphogenesis in the developing mammalian heart (vol 223, pg 266, 2000). Dev Biol. 2000;225:266-.

[37] Anderson RH, Webb S, Brown NA, Lamers W, Moorman A. Development of the heart: (2) - Septation of the atriums and ventricles. Heart. 2003;89:949-58.

[38] Aurigemma GP, Sharma M, Sweeney A, Sadler DB, Meyer TE, Gaasch WH. Extent and Velocity of Shortening Provide Similar Information About Chamber and Myocardial-Function in Hypertrophic and Normal Hearts. Circulation. 1995;92:3205-.

[39] Santhanakrishnan A, Miller LA. Fluid Dynamics of Heart Development. Cell Biochem Biophys. 2011;61:1-22.

[40] Taber LA, Zhang JM, Perucchio R. Computational model for the transition from peristaltic to pulsatile flow in the embryonic heart tube. J Biomech Eng-T Asme. 2007;129:441-9.

[41] Huang D, Swanson EA, Lin CP, Schuman JS, Stinson WG, Chang W, et al. Optical Coherence Tomography. Science. 1991;254:1178-81.

[42] Fercher AF, Hitzenberger CK, Kamp G, Elzaiat SY. Measurement of Intraocular Distances by Backscattering Spectral Interferometry. Opt Commun. 1995;117:43-8.

[43] Izatt JA, Choma MA. Theory of Optical Coherence Tomography. Biol Med Phys Biomed. 2008:47-72.

[44] Wieser W, Biedermann BR, Klein T, Eigenwillig CM, Huber R. Multi-Megahertz OCT: High quality 3D imaging at 20 million A-scans and 4.5 GVoxels per second. Opt Express. 2010;18:14685-704.

[45] Aguirre AD, Fujimoto JG. Optical Coherence Microscopy. Biol Med Phys Biomed. 2008:505-42.

[46] Tomlins PH, Wang RK. Theory, developments and applications of optical coherence tomography. J Phys D Appl Phys. 2005;38:2519-35.

[47] Raffel M, Willert C, Wereley ST, Kompenhans J. Particle Image Velocimetry A Practical Guide Second Edition Introduction. Exp Fluid Mech. 2007:1-13.

[48] Santiago JG, Wereley ST, Meinhart CD, Beebe DJ, Adrian RJ. A particle image velocimetry system for microfluidics. Exp Fluids. 1998;25:316-9.

[49] Adrian RJ. Particle-Imaging Techniques for Experimental Fluid-Mechanics. Annu Rev Fluid Mech. 1991;23:261-304.

[50] Prasad AK. Particle image velocimetry. Curr Sci India. 2000;79:51-60.

[51] Jensen KD. Flow Measurements. J Braz Soc Mech Sci & Eng. 2004;26:400-19.

[52] Aguirre AD, Hsiung P, Ko TH, Hartl I, Fujimoto JG. High-resolution optical coherence microscopy for high-speed, in vivo cellular imaging. Opt Lett. 2003;28:2064-6.

[53] Lee KS, Thompson KP, Meemon P, Rolland JP. Cellular resolution optical coherence microscopy with high acquisition speed for in-vivo human skin volumetric imaging. Opt Lett. 2011;36:2221-3.

[54] Dubois A, Vabre L, Boccara AC, Beaurepaire E. High-resolution full-field optical coherence tomography with a Linnik microscope. Appl Optics. 2002;41:805-12.

[55] Liu LB, Gardecki JA, Nadkarni SK, Toussaint JD, Yagi Y, Bouma BE, et al. Imaging the subcellular structure of human coronary atherosclerosis using micro-optical coherence tomography. Nat Med. 2011;17:1010-U132.

[56] Ding ZH, Ren HW, Zhao YH, Nelson JS, Chen ZP. High-resolution optical coherence tomography over a large depth range with an axicon lens. Opt Lett. 2002;27:243-5.

[57] Leitgeb RA, Villiger M, Bachmann AH, Steinmann L, Lasser T. Extended focus depth for Fourier domain optical coherence microscopy. Opt Lett. 2006;31:2450-2.

[58] Aguirre AD, Nishizawa N, Fujimoto JG, Seitz W, Lederer M, Kopf D. Continuum generation in a novel photonic crystal fiber for ultrahigh resolution optical coherence tomography at 800 nm and 1300 nm. Opt Express. 2006;14:1145-60.

[59] Wang YM, Zhao YH, Nelson JS, Chen ZP, Windeler RS. Ultrahigh-resolution optical coherence tomography by broadband continuum generation from a photonic crystal fiber. Opt Lett. 2003;28:182-4.

[60] Povazay B, Bizheva K, Unterhuber A, Hermann B, Sattmann H, Fercher AF, et al. Submicrometer axial resolution optical coherence tomography. Opt Lett. 2002;27:1800-2.

[61] Center TaA. Application Note Supercontinuum Generation in SCG-800 Photonoc Crystal Fiber. Newport Corporation. p. 9.

[62] Durnin J, Miceli JJ, Eberly JH. Diffraction-Free Beams. Phys Rev Lett. 1987;58:1499-501.

[63] McGloin D, Dholakia K. Bessel beams: diffraction in a new light. Contemp Phys. 2005;46:15-28.

[64] Chen Y, Liu JTC. Characterizing the beam steering and distortion of Gaussian and Bessel beams focused in tissues with microscopic heterogeneities. Biomed Opt Express. 2015;6:1318-30.

[65] Fahrbach FO, Simon P, Rohrbach A. Microscopy with self-reconstructing beams. Nat Photonics. 2010;4:780-5.

[66] Fahrbach FO, Rohrbach A. Propagation stability of self-reconstructing Bessel beams enables contrast-enhanced imaging in thick media. Nat Commun. 2012;3.

[67] Olympus. Knowledge: Depth of Focus. In: Focus Do, editor.2017.

[68] Wang R, Yun JX, Yuan XC, Goodwin R, Markwald RR, Gao BZ. Megahertz streak-mode Fourier domain optical coherence tomography. J Biomed Opt. 2011;16.

[69] Lorenser D, Singe CC, Curatolo A, Sampson DD. Energy-efficient low-Fresnel-number Bessel beams and their application in optical coherence tomography. Opt Lett. 2014;39:548-51.

[70] Photonics R. Chromatic Dispersion. RP Photonics Encyclopedia2017.

[71] Wojtkowski M, Srinivasan VJ, Ko TH, Fujimoto JG, Kowalczyk A, Duker JS. Ultrahigh-resolution, high-speed, Fourier domain optical coherence tomography and methods for dispersion compensation. Opt Express. 2004;12:2404-22.

[72] Nienhuys H-K. Prism-compressor. XFig. Wikipedia2006.

[73] Sia SK, Whitesides GM. Microfluidic devices fabricated in poly(dimethylsiloxane) for biological studies. Electrophoresis. 2003;24:3563-76.

[74] Madadi H, Mohammadi M, Casals-Terre J, Lopez RC. A novel fabrication technique to minimize poly(dimethylsiloxane)-microchannels deformation under high-pressure operation. Electrophoresis. 2013;34:3126-32.

[75] Deplaine G, Safeukui I, Jeddi F, Lacoste F, Brousse V, Perrot S, et al. The sensing of poorly deformable red blood cells by the human spleen can be mimicked in vitro. Blood. 2011;117:E88-E95.